Applied Catalysis B: Environmental 288 (2021) 119983

Contents lists available at ScienceDirect

Applied Catalysis B: Environmental

journal homepage: www.elsevier.com/locate/apcatb

Experimental and theoretical investigation of the control and balance of active sites on oxygen plasma-functionalized $MoSe_2$ nanosheets for efficient hydrogen evolution reaction

Dezhi Xiao [a], De-Liang Bao [b,c], Xiongyi Liang [a], Ying Wang [a], Jie Shen [d], Cheng Cheng [d], Paul K. Chu [a,*]

[a] Department of Physics, Department of Materials Science and Engineering, and Department of Biomedical Engineering, City University of Hong Kong, Tat Chee Avenue, Kowloon, Hong Kong, China
[b] Department of Physics and Astronomy, Vanderbilt University, Nashville, Tennessee 37235, USA
[c] Institute of Physics and University of the Chinese Academy of Sciences, Chinese Academy of Sciences, Beijing, 100190, China
[d] Institute of Plasma Physics, Chinese Academy of Sciences, Hefei, 230031, China

ARTICLE INFO

Keywords:
Plasma functionalization
Oxygen doping
Ion energy and flux
Molecular dynamics calculation
Hydrogen evolution reaction

ABSTRACT

Plasma functionalization is an effective method to improve the electrocatalytic activity of catalysts for the hydrogen evolution reaction (HER), but the relationship between the plasma and catalytic activity is not clear. Herein, oxygen plasma processing is conducted on $MoSe_2$ nanosheets and the effects of the plasma parameters including ion energy and radical flux are investigated by plasma simulation and molecular dynamics (MD) to fathom the interactions between the plasma and catalyst. A moderate ion energy and flux produce doping effects leading to proper replacement of Se sites by oxygen atoms to balance vacancy generation. Consequently, the HER characteristics are improved as exemplified by a small overpotential of 165 mV at 10 mA cm^{-2} and Tafel slope of 55.2 mV dec^{-1}. Based on first-principles density-functional theory calculation, increased polarization and state density distributions close to the Femi level introduced by oxygen and vacancies reduce the bandgap and ΔG_H at the Mo, Se, and O sites, consequently enhancing charge transfer between the catalyst and electrolyte. The results convey new fundamental knowledge about plasma surface functionalization of electrochemical catalysts and enable precise and optimal selection of plasma processing parameters to control and balance the active sites for efficient water splitting.

1. Introduction

Hydrogen energy featuring zero carbon emission and recycling of water is a potential candidate to replace traditional fossil fuels [1] and therefore, hydrogen production and utilization are hot topics in clean energy research [2,3]. Hydrogen can be produced by different techniques and one of the attractive means is electrochemical water splitting [4]. Noble metals such as platinum are popular catalysts for the hydrogen evolution reaction (HER) in water splitting but their scarcity and high cost hinder commercial application [5,6]. Therefore, alternative catalysts such as two-dimensional (2D) transition metal dichalcogenides (TMDs) which possess tunable crystalline and electronic structures as well as plenty of active sites have been explored [7–10]. In addition, optimization of the heterojunctions and defect engineering have been shown to improve the catalytic activity of TMDs in water splitting [11].

Plasma surface functionalization is an effective means to perform defect engineering, alter the surface morphology, and dope catalysts [12,13]. Both low-pressure and atmospheric-pressure plasma processes have been investigated [14–17]. For example, reactive plasma doping of polymetallic compounds such as nickel-based and cobalt-based metal oxides and layered double hydroxides has been shown to improve the electrochemical activity [18–20]. However, the actual influence of the dopants on the electrocatalytic activity is dubious because many elements coexist in the catalyst and electrochemical reactions are quite complicated to clarify. In contrast, TMDs with binary compound properties and tunable structures yield good effects after plasma surface modification because the electronic bandgap and Gibbs free energy can

* Corresponding author.
E-mail address: paul.chu@cityu.edu.hk (P.K. Chu).

https://doi.org/10.1016/j.apcatb.2021.119983
Received 10 November 2020; Received in revised form 16 January 2021; Accepted 4 February 2021
Available online 16 February 2021

be altered by plasma-induced defects and dopants [14,21,22]. Nevertheless, the different roles played by reactive plasmas (e.g. O_2 and N_2) and inert plasmas (Ar, He, etc.) in surface modification of electrochemical catalysts are not well understood and consequently, the outcome of various plasma interactions such as doping, etching, and defect generation is sometimes confusing [17,23]. Moreover, although the water splitting efficiency of catalysts can indeed be improved by plasma surface modification, the underlying mechanism has seldom been studied and the precise influence of plasma parameters on the catalytic activity is still unclear. Particularly, precise control of the active sites by selecting the optimal plasma processing parameters is essential but not well understood [24]. Therefore, a comprehensive study of the interactions between plasmas and catalysts is essential to optimize the active sites in catalytic reactions.

In this work, a low-pressure oxygen capacitively-coupled plasma (CCP) is sustained by 13.56 MHz radio frequency in the power range between 10 W and 30 W to modify $MoSe_2$ nanosheets prepared on carbon felt to investigate the doping effects and influence of different plasma parameters such as the energy, density, and radicals. Different from an inert gas plasma, the oxygen plasma serves the dual functions of sputtering and doping and the dopant distribution and concentration are dictated by the ion energy and density of radicals. As illustrated in Fig. 1, the $MoSe_2$ nanosheets hydrothermally synthesized on carbon felt is fixed on the bias electrode of the plasma reactor and subjected to various plasma interactions including ion bombardment, ion implantation, diffusion, as well as reactions associated with the oxygen discharge. The oxygen discharge and interactions are analyzed by plasma simulation and molecular dynamics, and the effects are experimentally verified by X-ray photoelectron spectroscopy (XPS), transmission electron microscopy (TEM), Hall effect measurements and so on. Besides replacement of Se atoms by oxygen atoms, some vacancies at Se sites are not fully occupied by oxygen after sputtering by oxygen ions, which is confirmed by the hall measurements. According to density-functional theory calculation, oxygen doping and vacancy formation increase the active sites, promote the conductivity, and reduce the Gibbs free energy (ΔG_H) to enable easier hydrogen adsorption. However, over-doping deteriorates the HER performance due to over-replacement of Se atoms by oxygen atoms giving rise to less active sites and larger ΔG_H. Therefore, the proper plasma ion energy and flux are crucial to balancing oxygen doping and vacancy generation. Our results reveal that the 20 W oxygen plasma treatment yields the best HER activity and enrich our understanding of the effects of plasma surface functionalization on the electrochemical properties of catalysts.

2. Experimental section

2.1. $MoSe_2$ nanosheets synthesis

Commercial $Na_2MoO_4{\cdot}2H_2O$, selenium powder, and $NaBH_4$ were purchased from Sigma Co., Ltd. and used without purification. The $MoSe_2$ nanosheets were fabricated on a piece of carbon felt by the conventional hydrothermal technique. In brief, 360 mg of Se powder, 440 mg of $Na_2MoO_4{\cdot}2H_2O$, and 60 mg of $NaBH_4$ were dissolved in 30 mL of distilled water and 30 mL of ethanol. The solution was put in a stainless steel autoclave together with carbon felt, sealed, and heated to 220 °C for 18 h. The $MoSe_2$ nanosheets were produced by annealing at 700 °C in argon for 2 h and dried at 65 °C for 12 h.

2.2. $MoSe_2$ thin film fabrication

To measure the carrier density and conductivity of $MoSe_2$ after the plasma treatment, the $MoSe_2$ film with a thickness of about 30 nm was deposited on glass at room temperature at a pressure of 10 m T using a radio-frequency (RF) power of 50 W (applied to the $MoSe_2$ target) on the physical vapor deposition (PVD) equipment manufactured by AJA International Inc. (USA).

2.3. Plasma functionalization processing

The annealed $MoSe_2$ nanosheets and films were transferred to the multifunctional plasma processing system made by the AJA International Inc. (USA) and treated for 600 s using radio frequency (13.56 MHz) power settings of 0 W, 10 W, 20 W, or 30 W. The pressure was 20 m T and oxygen flow rate was 20 sccm. The $MoSe_2$ film after the plasma treatment was vacuum annealed at 200 °C for 30 min for comparison.

2.4. Materials characterization

X-ray diffraction (XRD) was conducted on the Philips X'Pert Pro with Cu K_α irradiation and scanning electron microscopy (SEM) and transmission electron microscopy (TEM) were performed on the Thermo-Scientific and FEI Tecnai G2 F20, respectively. X-ray photoelectron spectroscopy (XPS) was carried out on the Thermo Scientific™ K-Alpha™ equipped with monochromatic Al K_α X-ray and Raman scattering was done on the HORIBA Scientific Lab RAM HR Raman spectrometer equipped with a 514.5 nm green laser. UV–vis double-beam spectrophotometry was performed on the Dynamic Model HALO DB-20 and Ramé-hart 500 was employed to measure the surface contact angles. The Se vaccines were evaluated by electron paramagnetic resonance (EPR, Bruker A300 EPR spectrometer). A standard probe station with an

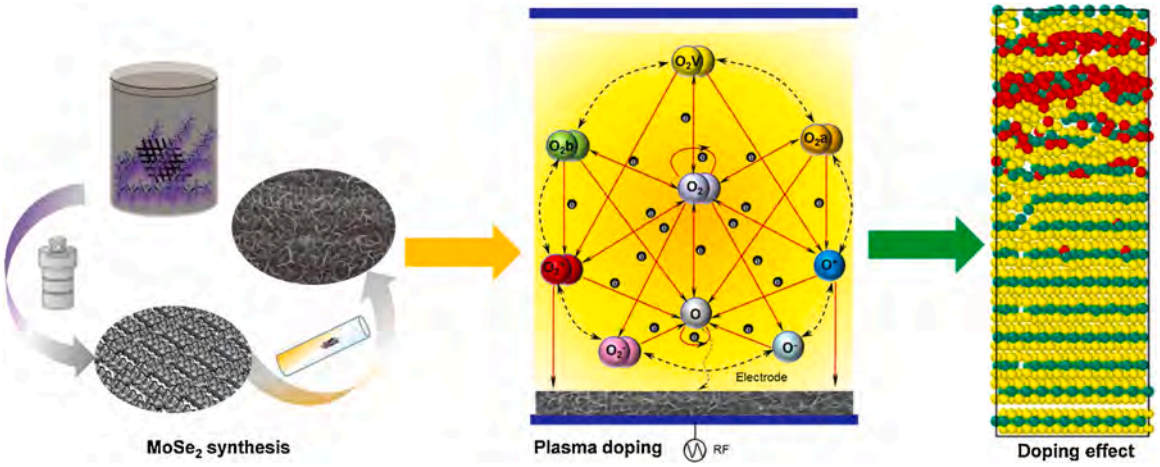

Fig. 1. Schematic illustration of the preparation of the $MoSe_2$ nanosheets, plasma surface functionalization using an oxygen discharge, as well as doping effects.

Agilent 4155C semiconductor analyzer (Agilent Technologies, Santa Clara, CA, USA) was used for the two-probe measurements. Atomic force microscopy (AFM) was performed on the Veeco DiMultimode and the Ecopia HMS-5300 Hall Effect measurement system was used in the carrier and conductivity measurements.

2.5. Electrochemical assessment

The electrochemical properties were determined on the CHI 6144D electrochemical workstation (CH Instruments, Inc. Shanghai) using the standard three-electrode configuration in which the $MoSe_2$ nanosheets on carbon felt, Ag/AgCl, and carbon graphite rod were the working, reference and counter electrodes, respectively. Linear scan voltammetry (LSV) was conducted at a scanning rate of 5 mV s^{-1} and cyclic voltammetry (CV) was performed at scanning rates from 10 mV to 100 mV and 0.15 V to 0.25 V. The electrochemical impedance spectroscopy (EIS) data were fitted with the simplified Randles circuit. All the electrochemical measurements were performed in 0.5 M H_2SO_4 and the potentials were calibrated and referenced to the reversible hydrogen electrode (RHE) based on the following equation: $E_{RHE} = E_{SCE} + 0.242\ V + 0.059\ pH$. The electrochemical double layer capacitances (C_{dl}) and per-site turnover frequency (TOF) were derived out according to the methodology described in previous reports [25,26].

2.6. Simulation of oxygen discharge, and interactions on $MoSe_2$ nanosheets

Plasma simulation was performed by solving the one-dimensional fluid model with the COMSOL Multiphysics software and the plasma reactions including excitation, ionization, dissociation, and collisions are summarized in Table S2 [27,28]. The pressure used was consistent with the experiments and the gas temperature was 300 K. More detailed descriptions of the various functions used in the computation such as the particle reactions, drift diffusion, energy transfer, and interactions under an electric field for species generated in the plasma can be found from related references [29,30].

Oxygen doping was simulated by the molecular dynamics code implemented with the LAMMPS (Large-scale Atomic/Molecular Massively Parallel Simulator) package [31]. 14 layers of $MoSe_2$ in the z-direction, 10 layers in the y-direction, and 1 layer in the x-direction were considered in the model. The oxygen energy and flux were derived from the plasma simulation results and atoms were injected into the $MoSe_2$ layers vertically in the z-direction regardless of the trajectories in the lateral directions of the x and y axes. The oxygen atom was initially positioned at 0.5 nm above the top layer in the z-direction. The temperature was 300 K and the bottom layer was fixed by ignoring the force generated by particle movement to avoid loss of oxygen atoms from the system. The Stillinger-Weber (SW) interatomic potential functions were considered for the interactions between oxygen atoms [32] and $MoSe_2$, and the SW potential parameters were extracted from the literature [33]. To visualize the particle movement and doping effects, the calculated results were imported to the OVITO software.

2.7. DFT calculation

First-principles calculation was performed using the Vienna ab initio simulation package (VASP) based on the density-functional theory (DFT) and the electron-ion interactions were conducted by the projector augmented wave (PAW) potentials [34,35]. The generalized gradient approximation (GGA) in combination with the Perdew Burke Ernzerhof (PBE) functional was adopted to describe the exchange-correlation interactions and the Van der waals (vdW) interactions were considered by the Grimme's DFT-D3 method. All the models were forced to a self-consistent accuracy of 10^{-5} eV. The kinetic energy cut-off of 450 eV for the plane-wave basis restriction and K-points were taken under Monkhorst-Pack for Brillouin-zone integration [36,37]. A sufficient vacuum slab of 15 Å was implemented to avoid interactions between adjacent layers and the $MoSe_2$ monolayer was calculated with the relaxed lattice constants of a = b =3.32 Å. To calculate the electronic properties and hydrogen evolution activity, a 4 × 4×1 supercell was used. The HER characteristics were evaluated by ΔG_{H^*} defined as $\Delta G_{H*} = \Delta E_H + \Delta E_{ZPE} - T\Delta S_H$ [38], where ΔE_H, ΔE_{ZPE}, S_H are the differential hydrogen adsorption energy, change in the zero point energy, and entropy between adsorbed hydrogen and molecular hydrogen in the gas phase, respectively, and T is the temperature. The term $T\Delta S_H$ is taken as -0.205 eV for the gas phase standard state (300 K, 1 bar).

3. Results and discussion

3.1. Characterizations of catalysts

The $MoSe_2$ nanosheets hydrothermally synthesized on carbon felt and treated with the oxygen plasma using different power settings are characterized by X-ray diffraction (XRD). As shown in Fig. 2a, typical diffraction peaks from $MoSe_2$ are observed besides that from the carbon felt (CF). When the plasma power is increased to 20 W, the peaks show little changes, but some small peaks related to molybdenum oxide appear after the 30 W plasma treatment due to over-doping and excessive oxygen implantation [39,40]. The intensity of the (002) peak decreases gradually with increasing power and a shift to a smaller angle is shown in Fig. S1a. The reason for the changes is that oxygen coverts $MoSe_2$ into molybdenum oxide such as MoO_2 and MoO_3, which hybridize the crystal lattice [41–43]. Fig. 2b displays the Raman scattering results and similar to XRD, two small peaks appear at the high wavenumber from the 30 W sample arising from molybdenum oxide. In addition, red-shift occurs with wavenumber shifting to a smaller value as shown in the inset implying structural change. According to the literature [44,45], the oxygen plasma introduces oxygen into the $MoSe_2$ crystal, alters dielectric screening in the environment, and restores the force between adjacent $MoSe_2$ layers, consequently affecting the vibrational frequencies and producing the red-shift. UV–vis spectrophotometry is performed to determine the change in the electronic bandgap (Fig. S1b). As shown in Fig. 2c, the bandgap decreases from 1.21 eV of the untreated sample to 1.12 eV of the 20 W sample providing evidence that oxygen plasma modification improves the $MoSe_2$ conductivity.

The composition of $MoSe_2$ after plasma modification is determined by X-ray photoelectron spectroscopy (XPS). As shown in Fig. 2d, compared to the pristine $MoSe_2$ which exhibits Mo^{4+} as indicated by the peaks of Mo 3d 5/2 at 232.1 eV and Mo 3d 3/2 at 228.7 eV as well as the small peak at 230.3 eV of Mo^{5+} arising from weak air oxidization, the high valence state of Mo^{6+} and more Mo^{5+} emerge from the 20 W and 30 W samples because of oxygen insertion after the plasma treatment [22,42,46]. More oxygen is incorporated after 30 W plasma exposure (Table S1) due to the higher ion energy and density. Additionally, a shift in the binding energy arising from changes in the crystal lattice and dielectric screening is observed [47], as indicated by the shift of the Mo 3d 3/2 peak from 232.13 to 232.44 eV and 232.32 eV, respectively in Fig. S1c. A similar phenomenon is observed from Se 3d in Fig. 2e. Different from natural oxidization in air, Fig. 2f discloses the extent of energetic oxygen ion implantation into $MoSe_2$. Compared to that at 532.5 eV stemming from MoO_3 and surface contamination on the pristine $MoSe_2$ [48,49], the new state of O 1s at about 531.0 eV after plasma modification originates from sub-surface oxygen confirming the existence of MoO_2 with a distorted rutile crystal structure which has metallic conductivity and high electrochemical activity [50,51]. The peak shift to smaller binding energy after the 30 W treatment suggests more oxygen incorporation and larger implantation depth [48,52] and the results are consistent with the theoretical results to be discussed later (Fig. 5).

Scanning electron microscopy (SEM) is performed to investigate the morphological change after the plasma treatment. As shown in Fig. S2a, the $MoSe_2$ nanosheets are uniformly distributed on the carbon felt and the SEM images in Figs. 3b and S2b disclose that the morphology is only

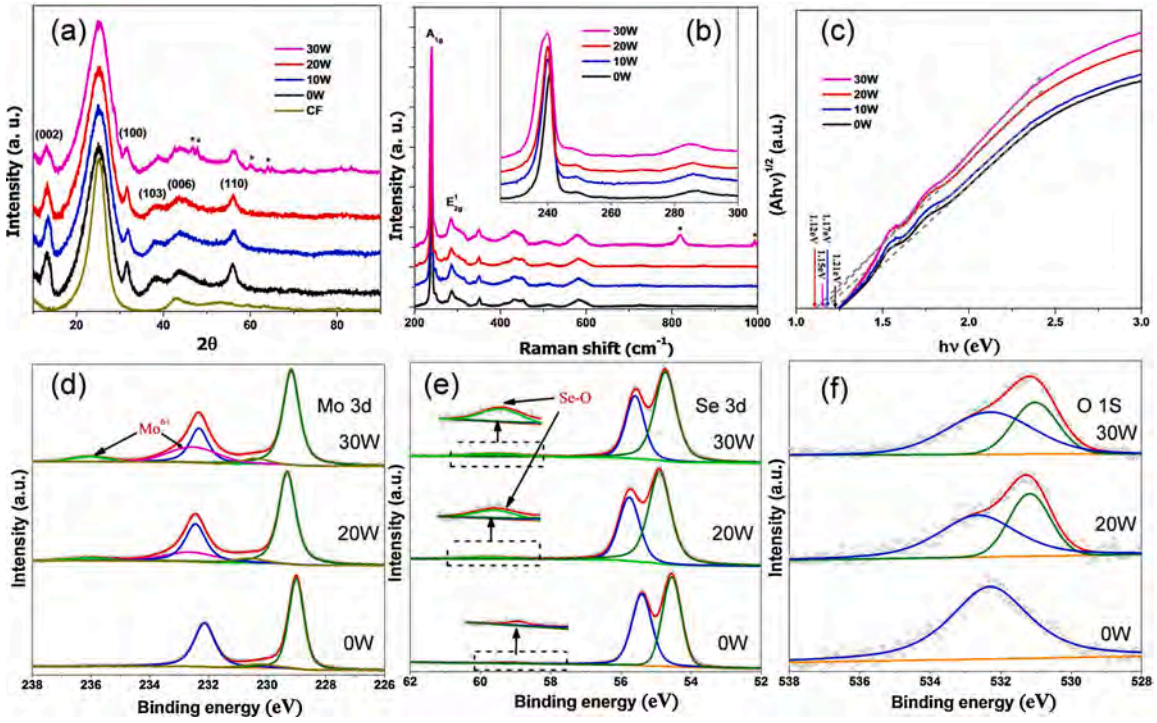

Fig. 2. Characterization of $MoSe_2$ nanosheets modified using different discharge power settings: (a) XRD patterns, (b) Raman scattering spectra, (c) Bandgaps derived by UV–vis spectrophotometry, and XSP spectra of (d) Mo 3d, (e) Se 3d, and (f) O 1s.

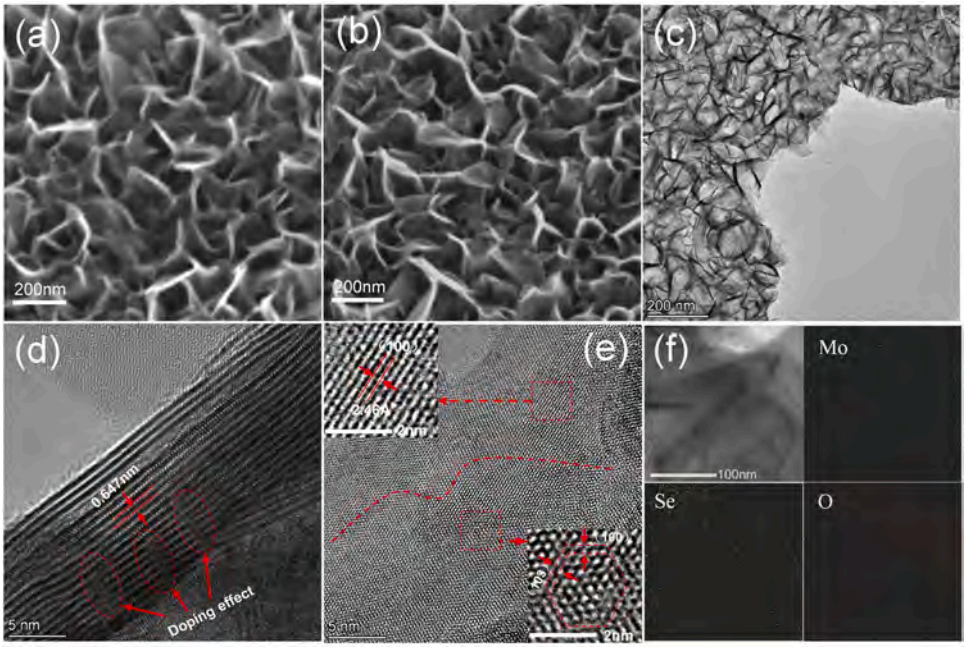

Fig. 3. SEM images of $MoSe_2$ modified using power settings of (a) 0 W and (b) 20 W; TEM image of $MoSe_2$ modified using 20 W: (c) Low-resolution TEM image, (d and e) High-resolution TEM images, and (f) EDS elemental maps.

slightly altered by the oxygen plasma in contrast to the pristine sample without modification (Fig. 3a). Owing to the complicated effects of physical collisions, electron transfer, and ion-ion recombination in the oxygen discharge [27], the oxygen plasma has a smaller ion density and flux than the argon discharge as shown in Figs. S3a-b and consequently, weak etching is observed relative to an argon plasma (Fig. S3c). Furthermore, different from the argon plasma treatment which produces only the physical effect of sputtering, the oxygen plasma also introduces chemical modification and creates an oxygen in-depth distribution. The elemental maps in Fig. S4 reveal increasing oxygen concentrations with discharge power besides the elemental distributions of C, Mo, and Se with moderate oxygen doping after the 20 W treatment.

Fig. 3c depicts the low-magnification TEM image after oxygen plasma modification and vertical nanosheets are observed similar to the SEM observation and the insignificant morphological change indicates that etching is minimal. The high-resolution TEM image in Fig. 3d

reveals a layer spacing of 0.647 nm corresponding to the $MoSe_2$-(002) plane. The blurred areas interrupting the normal lattice indicated by the red circles in Fig. 3d disclose the plasma-induced lattice damage which is also validated by the comparison before and after the plasma treatment shown in Fig. S5a. The crystal lattice of $MoSe_2$ after oxygen plasma modification in Fig. 3e shows the conversion of the typical 2H-$MoSe_2$ magnified at the bottom right corner to MoO_2 shown at the top left corner [50]. The converted structure is corroborated by Figs. S5b-d and fast Fourier transform (FFT) image in Fig. S5e, demonstrating MoO_2 formation by plasma-induced oxygen doping [40,43]. Oxygen incorporation after plasma functionalization is also confirmed by the elemental maps in Fig. 3f. Besides oxygen doping, the defects produced by the plasma are evaluated by EPR measurements. As shown in Fig. S6, a higher intensity indicates more Se vacancies generated after the plasma treatment [17]. Combining the TEM observation and XPS and EPR results, oxygen doping from the plasma produces different states of oxide and the binding energy shift as well as vacancies stem from the interactions between the plasma and catalyst. Therefore, it is essential to unravel the mechanisms by investigating the plasma process on the catalyst.

3.2. *Mechanism studied by simulation of the oxygen discharge and doping process and Hall measurements*

Although there have been studies on the effects of plasma functionalization on the activity of electrocatalysts [12,14,16], the associated mechanisms and discrete effects of the various interactions are not well understood. A better understanding of the various plasma processes such as electron impact and radical collisions as well as properties such as radical species and ion energy is crucial to the design and preparation of catalysts by optimizing the effects of etching, doping, and defect generation under different plasma conditions. Here, the important plasma parameters including the energy, density, and radicals which affect sputtering, doping, and etching are investigated. Fig. S7 presents the reactions in the oxygen discharge including electron-impact excitation, ionization, dissociation and collisions and they are summarized in Table S2. Comparison between simulation and experimental results in Fig. S8 illustrates a CCP discharge. The electron densities in the plasmas sustained by different power settings are presented in Fig. 4a which indicates a dominant middle zone of the plasma as the source of ions and radicals. The characteristic drop above the electrode arises from plasma consumption including processes of ion bombardment and radical diffusion in the plasma sheath [29,53,54]. Fig. 4b shows the primary radicals and ions formed in plasma are influenced by the doping process through combination of ion bombardment, radical diffusion, and formation of the modified surface [27,55]. On account of the sharp potential drop across the sheath, the positive plasma potential in Fig. 4c forces ions to rapidly migrate from the central plasma zone to the electrode in energetic ion bombardment and ion implantation. However, owing to the reverse movement of positive and negative ions (Fig. 4b), the positive ion flux concentrates in the pre-sheath as shown in Fig. 4d and is consumed by negative ions (O^{2-}, O- and electrons) thus accounting for the weaker etching effects compared to an argon plasma (Figs. S3a-c). The electric field across the sheath on the electrode generated by the bias voltage (Fig. 4e) accelerates free positive ions in the pre-sheath to traverse the collisionless sheath to the catalyst surface resulting in oxygen ion implantation. The movement of ions and radicals in the chamber can also be observed by the collisional energy loss shown in Fig. 4f and Fig. S9a-b, in which ions are extracted from the plasma across the sheath into the materials accompanied by power dissipation and energy loss because of the strong interactions between the plasma and materials. By means of plasma simulation, the evolution of ions and radicals in the plasma can be determined.

Different from previous reports in which the catalysts are only exposed to the plasma "statically" [12,17,23], our samples experience extra energetic ion interactions arising from the sample bias which can be utilized to tune the dopant concentration and distribution. In our experiments, the $MoSe_2$ nanosheets are fixed on the biased electrode as shown in Fig. 1 and owing to the electric field across the plasma sheath, oxygen ions and charged particles are accelerated to bombard the nanosheets as shown in Fig. S10a leading to oxygen doping of the $MoSe_2$ layers together with sputtering and defect formation, which depend of the ion energy, density, and radicals of the plasma species as shown in Figs. 4a-f. These effects are accentuated as the discharge power goes up. To evaluate the influence of these parameters on the catalytic properties, multiple aligned $MoSe_2$ layers are used to simulate the nanosheets

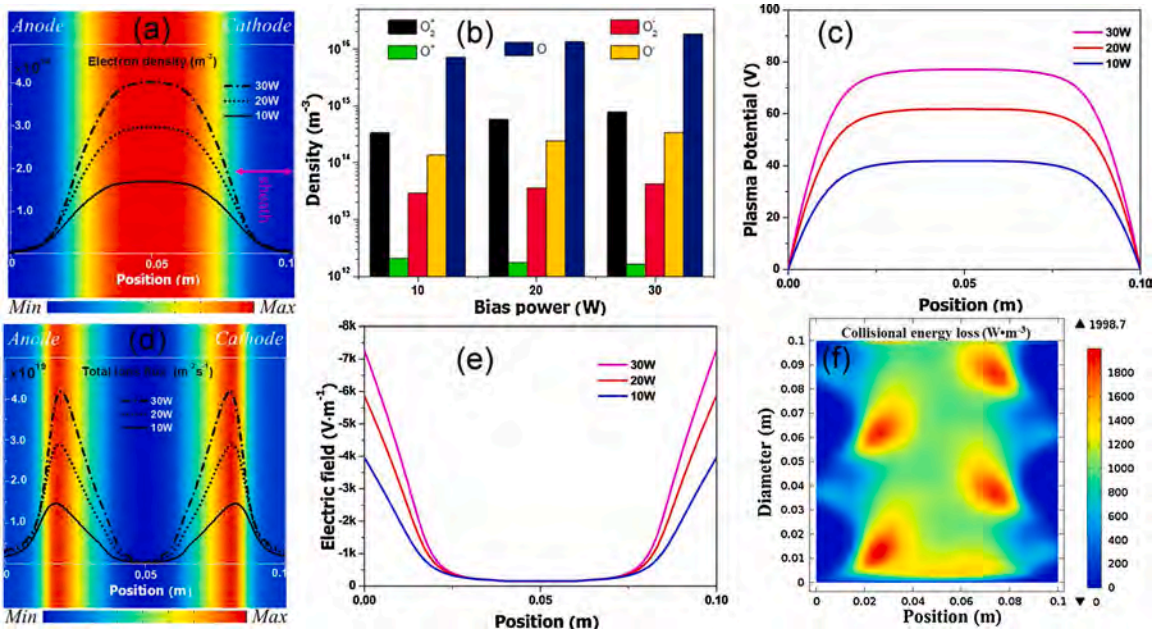

Fig. 4. Plasma simulation of different oxygen discharges: (a) Electron density distributions, (b) Primary ions and radicals taking part in the interactions between the plasma and catalyst, (c) Plasma potential distribution, (d) Ion fluxes to the electrode, (e) Electric field distributions, and (f) Collision energy loss companied by migration of ions and radicals in the 20 W plasma process.

during plasma exposure. Molecular dynamics (MD) simulation is performed using the LAMMPS package by solving Newton's equations of motion [32,33,56]. Fig. 5a presents the surface evolution of the $MoSe_2$ nanosheets taking into the ion energy and flux based on results in Fig. 4. Sputtering and lattice destruction are observed after plasma exposure compared with the initial state and oxygen atoms are present at the sub-surface of the 10 W sample after stripping the surface atoms. Compared to the 10 W sample, oxygen diffuses to greater depths in the 20 W and 30 W samples together with more substantial sputtering and structural damage as shown by the snapshots of surface evolution, which are in line with the observation in Fig. 3d. The ion bombardment and radical diffusion affect oxygen doping synergistically that energetic ions penetrate the molecular layers and sputter away Se atoms. At the same time, oxygen radicals diffuse to the Se sites forming oxide. However, the radicals have less energy without acceleration by the electric field and are initially confined in a shallow zone before gradually diffusing into a deeper zone. More heat and energy are consumed on the surface to benefit formation of MoO_3, and MoO_2 is produced by replacing Se atoms in the deeper layers. In addition, the Se sites not occupied by oxygen atoms in the deeper zone remain as vacancies as shown in Fig. 5a. As a result, different valence-state oxides as well as vacancies are mixed in the oxygen-doped region. More oxygen atoms are introduced in the 30 W treatment due to the larger ion energy and flux. The changes in oxygen concentrations with power shown in Fig. 5b are comparable to the XSP results in Table S1 by taking into account of the nanosheet thickness (Figs. S10b-c). The oxygen depth distribution along the vertical orientation of the nanosheet is displayed in Fig. S10d and the corresponding $MoSe_2$ layers are shown in Fig. 5b considering the main doped region. The dopant depth is also studied by the Monte Carlo code and the results of the 30 W sample in Fig. S11 are consistent with those obtained by the LAMMPS code. The overall results reveal that over-doping brought about by larger ion energy and flux (30 W power) introduces excessive oxygen atoms compared to doping using a medium power of 20 W, but 10 W does not produce sufficient effects.

The electrical properties of the catalyst after plasma functionalization are critical to the electrochemical activity as better conductivity leads to better HER performance. It is noted that the electrical properties of catalysts without electrolytes have rarely been studied [13,16,18]. Fig. S12 displays the I–V and resistance results indicating promoted conductivity after the plasma treatment. However, the two-probe measurement determined by the carbon fiber in two dimensions (Fig. S12a) cannot calibrate the current and exclude the contact resistance thus producing resistance values that vary significantly with the voltage (Fig. S12c). Additionally, the carrier type (i.e. n or p-type) of $MoSe_2$ after the plasma treatment cannot be determined either. To better determine the carrier type, the relationship between the carrier concentration and conductivity as well as influence of oxygen doping on vacancies and physical changes of $MoSe_2$ is assessed by Hall measurement which is more precise and sensitive to get physical information by affiliating with the four-probe detection calibrating all the electrical parameters in our case [56]. A smooth $MoSe_2$ film with a thickness of 30 nm is prepared on a glass substrate (Fig. S13a) to support the four probes for the Hall measurements comparatively revealing the mechanisms of plasma functionalization of $MoSe_2$ nanosheets.

The negative value of the carrier concentration in Fig. 6a indicates the n-type semiconductor property of $MoSe_2$ [14]. The concentration increases with the discharge power before 30 W but conversely after that on account of over-doping at high power which produces more stable oxide because of more energy diffusion and consumption and inhibition of the free movement of electrons. The electron mobility reflects the capacity of electron transfer and enhanced mobility after the proper plasma exposure is shown in Fig. 6a. The best results are observed for 30 W because the glass substrate has poorer conductivity compared to the carbon felt. By integrating the carrier concentration and mobility, the conductivity is summarized in Fig. 6b which presents a similar trend and improvement. To confirm the vacancies in the layers, Hall measurements are carried out from the samples after vacuum annealing. Figs. 6a-b indicate that the carrier concentration, mobility and conductivity decrease after annealing due to recombination of vacancies by oxygen or Se atoms at the high temperature. As shown in Fig. 6c, Se vacancies in the deeper zone and disordered lattice arising from ion bombardment and sputtering remain before annealing. Nonetheless, high-temperature annealing facilitates oxygen diffusion and Se rearrangement as shown in Fig. 6d and consequently, the vacancies are re-occupied by oxygen or Se atoms. Therefore, the amount of vacancies can be estimated by observing the change in the carrier concentration before and after annealing during the Hall measurement because Se vacancies can be recombined after high-temperature annealing. The I–V measurement in Fig. S13b reveals reduced conductivity with a higher sheet resistance after annealing. Moreover, self-heating and energy absorption at a larger power such as 50 W lead to over-doping and fewer vacancies and hence, there is inconspicuous difference in the carrier concentration and mobility before and after annealing (Fig. 6a).

3.3. Hydrogen evolution reaction performance

The hydrophilic properties of the samples after the oxygen plasma treatment are determined. As shown in Fig. S14a, the pristine $MoSe_2$ is hydrophobic but after oxygen plasma modification, the contact angles (Fig. S14b) indicate improved hydrophilicitility because of the enhanced polarity after oxygen incorporation which improves electron / proton transfer between the catalyst and electrolyte and ultimately the HER activity [45,57]. To examine the effects of plasma functionalization on the electrocatalytic activity, HER measurements are conducted in 0.5 M H_2SO_4 employing the calibrated three-electrode configuration. The polarization curves acquired by linear scan voltammetry (LSV) at a scanning rate of 5 mV s^{-1} in Fig. 7a demonstrate significant improvement in the HER properties after plasma functionalization. The best performance is observed from the 20 W sample, as exemplified by the smallest overpotential of −165 mV at 10 mA cm^{-2}, which is closest to that of the

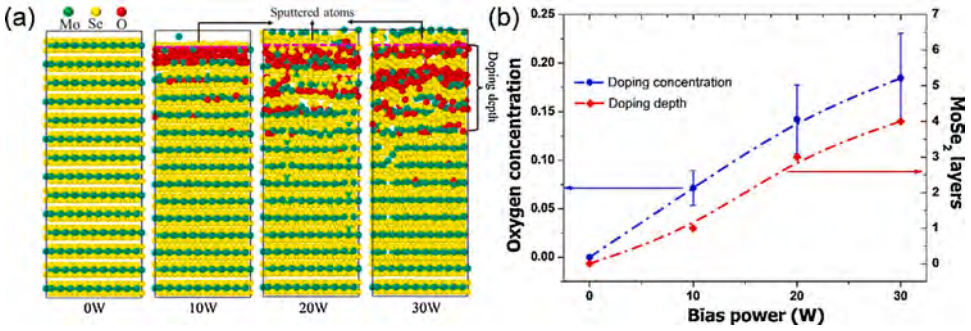

Fig. 5. Molecular dynamics (MD) simulation of oxygen doping for different oxygen discharges: (a) Snapshots of the oxygen doping evolution and (b) Oxygen concentrations and depths calculated by MD.

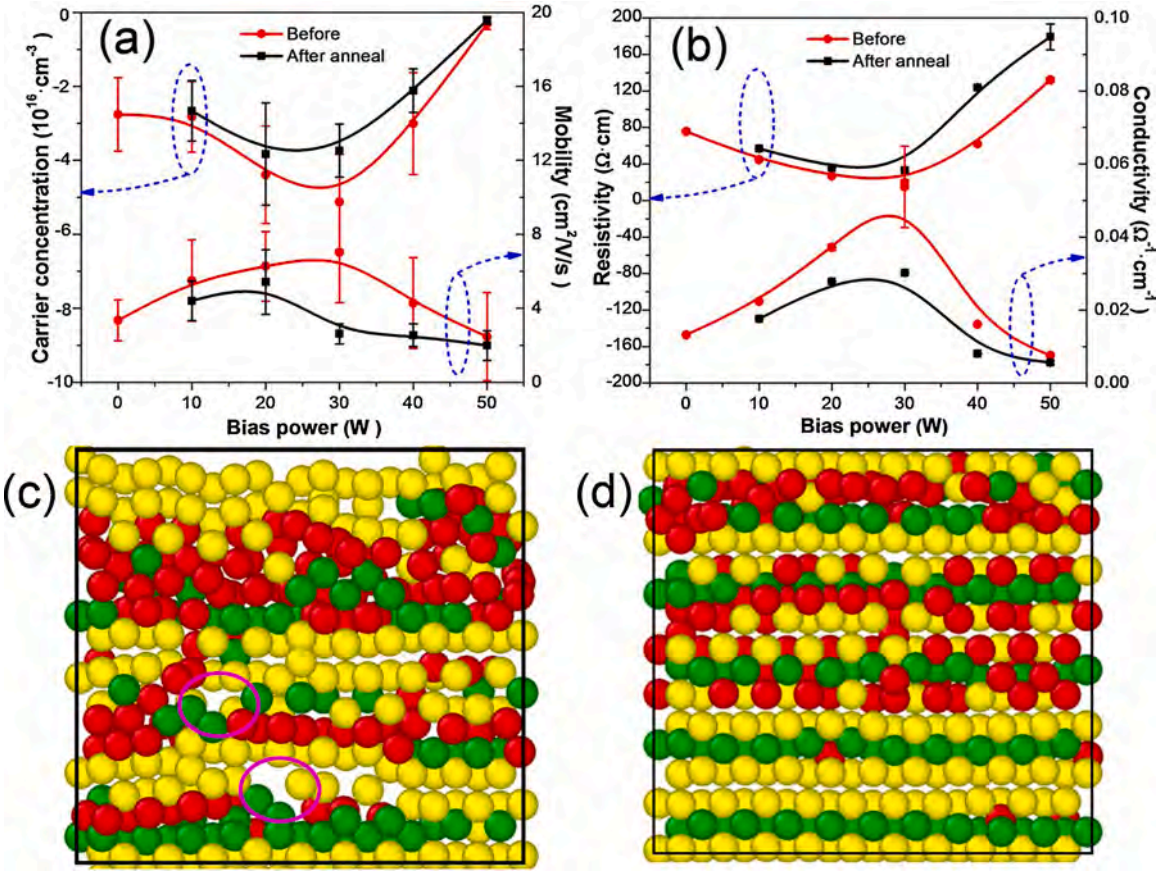

Fig. 6. Hall measurements: (a) Carrier concertation and electron mobility, (b) Conductivity and resistivity, (c) Disordered $MoSe_2$ lattice with vacancies after plasma exposure, and (d) Rearrangement of the $MoSe_2$ lattice after annealing.

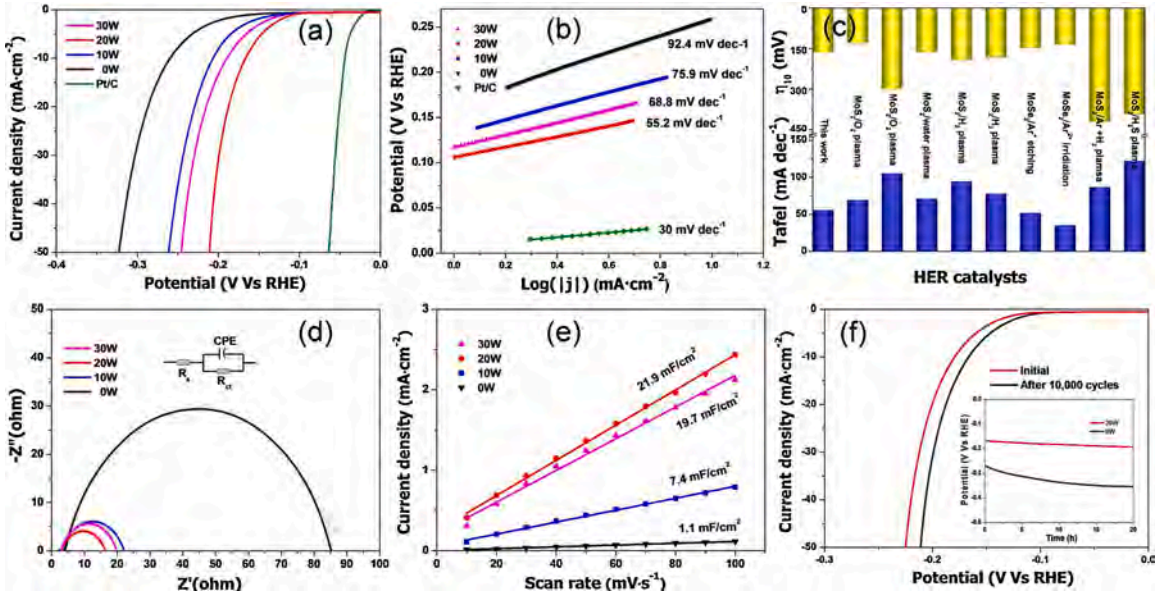

Fig. 7. HER characteristics of the catalysts: (a) LSV curves, (b) Tafel plots, (c) Overpotentials and Tafel slopes in comparison with other reported catalysts, (d) Nyquist plots derived by EIS, (e) Capacitive current densities at different scanning rates, and (f) Stability evaluation of the 20 W $MoSe_2$ sample.

Pt/C electrode, indicating fast electron transfer kinetics in ther redox reaction. Moreover, the smaller Tafel slope of 55.2 mV dec^{-1} observed from the 20 W sample in Fig. **7**b suggests larger a reaction rate and superior HER electrocatalytic activity benefiting from the embedded MoO_2 and vacancies in the subsurface layers [9,14,51]. The depressed electrocatalytic activities of the 10 W and 30 W samples can be attributed to either insufficient or excessive effects of oxygen incorporation as discussed above from the theoretical and experimental perspectives. The Tafel slope of the Pt/C catalyst (30 mV dec^{-1}) is similar to that reported previously confirming the consistency and validity between our and

previous results [14,51,58]. Compared to other metal-based catalysts such as layered double hydroxides (LDH) and metal-organic frameworks (MOF), the performance of the $MoSe_2$ is intermediate. However, these catalysts always contain more than two elements (e.g. Ni, Fe, Co, etc.) and the mechanisms responsible for the electrochemical activities are more complicated [59,60]. Therefore, it is more difficult to clarify the interactions between the catalyst and plasma using these other catalysts. For instance, a more mesoporous triangular-shaped Co-Fe-MOF structure is produced after annealing at a higher temperature comparing to the Ar-O_2 plasma treatment, but regular engraved NiFe-LDH holes are etched by a hot plasma (>500 °C) without lithography thus blurring the interactions between the catalyst and plasma [17,23]. All in all, $MoSe_2$ is easier to analyze because of fewer elements and stable structure after high-temperature annealing. By optimizing the plasma parameters to achieve optimal control of the active sites, $MoSe_2$ nanosheets deliver better HER performance in comparison with other molybdenum-based TMDs modified by different plasma techniques as shown in Fig. **7**c and Table S3.

Electrochemical impedance spectroscopy (EIS) is performed and the data are fitted by an equivalent circuit. As shown in Fig. 7d, the charge transfer resistance (R_{CT}) decreases after plasma doping to 16.3 Ω, 19.7 Ω, and 22.1 Ω corresponding to the 20 W, 30 W, and 10 W samples, respectively, which are much smaller than 85.5 Ω of the pristine $MoSe_2$ suggesting improved conductivity after plasma exposure. The combined EIS and Hall results indicate improved electrical properties by lowering the charge transfer resistance between the catalyst and electrolyte [14]. To evaluate the relationship between the catalytic properties and electrochemical active surface area (ECSA), cyclic voltammetry (CV) (Fig. S15) is conducted to calculate the electrochemical double-layer capacitance (C_{dl}) [42] in the potential range of 150–250 mV (vs. RHE) at scanning rates between 10 and 100 mV/s. The linearly fitted curves of C_{dl} in Fig. 7e show that the 20 W sample has the largest value of 21.9 m F cm^{-2} compared to the 30 W, 10 W, and pristine $MoSe_2$ which show 19.7 m F cm^{-2}, 7.4 m F cm^{-2}, and 1.1 m F cm^{-2} respectively, indicating larger ECSA and more catalytic active sites on the moderately oxygen-doped 20 W sample. The turnover frequency (TOF) is calculated to estimate the HER capability of the active sites by taking into account the LSV curves and C_{dl} [25]. As shown in Fig. S16, the TOF is improved after the plasma treatment and the best effect is again observed from the 20 W sample. The 30 W sample shows worse HER capability as more oxygen atoms are incorporated to occupy the vacancies and form high valence oxide which has a lower electrocatalytic activity as confirmed by Fig. 8. In the electrochemical measurements, moderate oxygen doping and the optimal amount of vacancies improve proton / electron transfer at the solid-liquid interface by improving the polarity and conductivity, implying that the amount of incorporated oxygen is crucial.

Besides the activity, the electrocatalytic stability of catalysts is an important factor [18]. The long-term stability test is carried out by replacing the Pt/C electrode with a graphite rod to avoid Pt/C dissolution and contamination to other electrodes [58]. The polarization curve of the 20 W sample after cycling for 10,000 cycles exhibits only small deterioration (Fig. 7f). Compared to the pristine sample, the minute drop in the inset figure after the test for 20 h is ascribed to minute surface oxidization in the acidic electrolyte due to protection by the modified surface layer on $MoSe_2$.

3.4. Analysis of the electrocatalytic activity by DFT calculation

To investigate the mechanism of the oxygen dopant and vacancies on the HER catalytic activity, first-principles density-functional theory (DFT) calculation is conducted by substituting Se atoms with O atoms because Se is sputtered more easily by oxygen ions as revealed by XPS. The simulation is performed by inserting one and two oxygen atoms into the system as shown in Fig. S17 to compare oxygen doping. In addition, an oxygen atom is inserted into a Se vacancy in the study (Fig. S18). The calculated bandgaps in Fig. 8a and Fig. S19 show smaller reduction after oxygen incorporation consistent with the UV–vis results in Fig. 2c. Compared to the pristine $MoSe_2$, a new density-of-states (DOS) peak appears near the valence band and shifts gradually to the Femi level as a result of the interactions between oxygen and Mo and Se lowering the energy barrier between the valence band and conduction band [61]. It reflects the enhanced density of active sites in HER. Different from oxygen doping only, the bandgap is significantly reduced when vacancies are introduced and a new DOS appears at the conduction band due to dangling electrons on the Mo atom. The extra active sites arise mainly from the dangling Mo atoms in the vacancy case compared to oxygen doping because Mo and O atoms play important roles in the new active sites similar to active sites at the Mo edge and O edge in MoO_2 [50]. The electron density distribution in Fig. S20 shows the effects of oxygen doping on charge transfer. There is an obvious enhancement on the

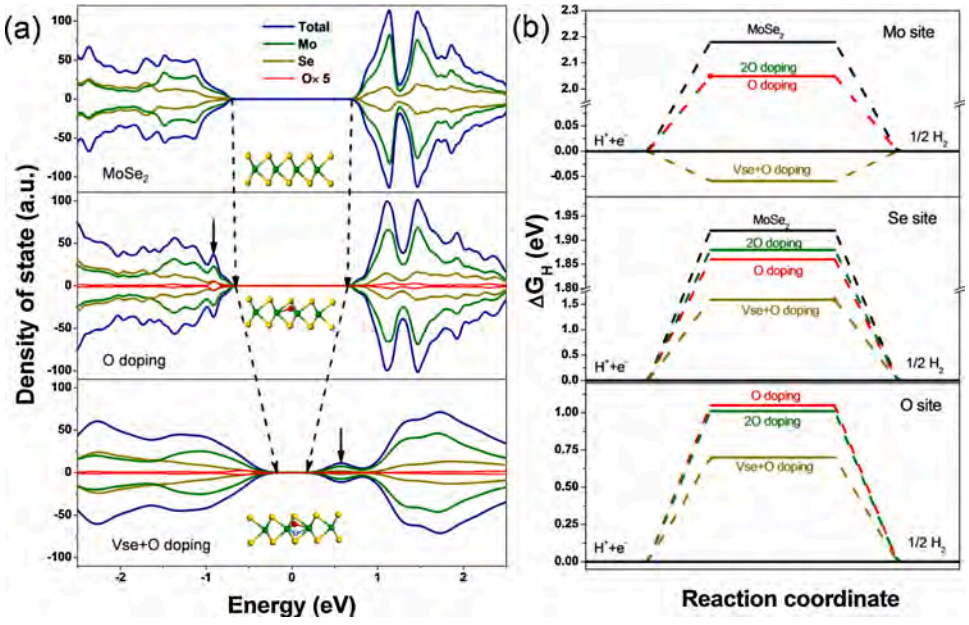

Fig. 8. DFT calculation results for different oxygen doping levels: (a) Density-of-state distribution and (b) ΔG_H at Mo, Se, O sites.
Methodology

electron distribution around the O edge compared to the Se edge, and the Bader charge on the O site (-1.25e$^-$) is almost two times higher than the charge on the Se site (-0.68e$^-$) indicating improved polarization and stronger adsorption of H^+ from the electrolyte leading to the better HER performance [61,62].

The effects of oxygen doping and vacancies on hydrogen adsorption are investigated by calculating ΔG_H for the different active sites (Fig. S17 and Fig. S18). As shown in Fig. 8b, $|\Delta G_H|$ decreases at the Mo and Se sites in both cases because of polarization and enhanced conductivity brought by the inserted oxygen atoms and vacancies, respectively [62,63]. However, no difference is observed from the Mo site in the cases of one and two oxygen atoms as Mo atoms are occupied fully with oxygen and selenium atoms. Although the oxygen active sites can further reduce $|\Delta G_H|$ because of the closer density distribution to the Femi level, $|\Delta G_H|$ at the Se site deteriorates when the doping concentration is further increased (e.g. 2O doping). Since Se atoms provide the prime active sites for HER in the $MoSe_2$ basal plane [14], excessive replacement of Se sites by oxygen atoms worsens the HER activity. Vacancy introduction reduces $|\Delta G_H|$ both at the Se site and O site. As summarized in Table S4, a proper balance between Se and O atoms as well as vacancy sites is crucial to the electrochemical activity and HER characteristics. The combination of oxygen doping and vacancies produced by the plasma contributes to the enhanced electrocatalytic activity and our results produce evidence that plasma surface modification is very helpful in boosting the performance of electrochemical catalysts in HER.

4. Conclusion

A capacitively-coupled oxygen plasma is applied to modify $MoSe_2$ nanosheets and the effects of the important plasma parameters such as the energy of ions and density of radicals on the HER activity are investigated. The increased polarity after oxygen incorporation improves the surface hydrophilicity of the materials and the synergistic effects rendered by the oxygen dopant and vacancies facilitate faster charge transfer between the catalyst and electrolyte and promote the conductivity and amount of active sites. However, over-doping is counter-productive because of vacancies reoccupation and excessive replacement of Se sites by oxygen atoms. Our results show that moderate ion energy and flux yield the optimal HER characteristics such as a small overpotential of 165 mV at 10 mA cm^{-2} and a smaller Tafel slope of 55.2 mV dec^{-1}. Theoretical simulation imparts information on not only the oxygen plasma discharge, but also migration of ions and radicals in the materials, which are used as initial parameters in the MD calculation to analyze the interactions between energetic oxygen species and $MoSe_2$ molecules. The theoretical results are consistent with the experimental observation. Based on the DFT calculation, oxygen and vacancy reduce ΔG_H at the Mo, Se and O sites as a result of increased polarization and also because the state density distribution is close to the Femi level. To achieve the best improvement, balanced substitution of Se by oxygen atoms and vacancies reservation are essential to the optimal control of the active sites control, which can be accomplished by tuning the plasma conditions. This study enriches our fundamental understanding of the interactions between plasmas and HER catalysts and the results also provide insights into the design and surface modification of high-performance catalysts for water splitting.

CRediT authorship contribution statement

Dezhi Xiao: Conceptualization, Methodology, Investigation, Writing - original draft. **De-Liang Bao:** Software, Visualization. **Xiongyi Liang:** Software, Visualization. **Ying Wang:** Data curation. **Jie Shen:** Formal analysis, Validation. **Cheng Cheng:** Formal analysis, Validation. **Paul K. Chu:** Supervision, Funding acquisition, Writing - review & editing.

Declaration of Competing Interest

The authors declare no competing interests.

Acknowledgments

This work was financially supported by the Hong Kong Scholars Program (XJ2018009) and City University of Hong Kong Strategic Research Grant (SRG) No. 7005505.

Appendix A. Supplementary data

Supplementary material related to this article can be found, in the online version, at doi:https://doi.org/10.1016/j.apcatb.2021.119983.

References

[1] J.A. Turner, Sustainable hydrogen production, Science 305 (2004) 972–974, https://doi.org/10.1126/science.1103197.
[2] D. Parra, L. Valverde, F.J. Pino, M.K. Patel, A review on the role, cost and value of hydrogen energy systems for deep decarbonisation, Renew. Sust. Energ. Rev. 101 (2019) 279–294, https://doi.org/10.1016/j.rser.2018.11.010.
[3] I. Staffell, D. Scamman, A. Velazquez Abad, P. Balcombe, P.E. Dodds, P. Ekins, N. Shah, K.R. Ward, The role of hydrogen and fuel cells in the global energy system, Energ. Environ. Sci. 12 (2019) 463–491, https://doi.org/10.1039/c8ee01157e.
[4] Q. Wang, K. Domen, Particulate photocatalysts for light-driven water splitting: mechanisms, challenges, and design strategies, Chem. Rev. 120 (2020) 919–985, https://doi.org/10.1021/acs.chemrev.9b00201.
[5] M.S. Fabera, J. Song, Earth-abundant inorganic electrocatalysts and their nanostructures for energy conversion applications, Energ. Environ. Sci. 7 (2014) 3519–3542, https://doi.org/10.1039/C4EE01760A.
[6] J. Zhang, T. Wang, P. Liu, Z. Liao, S. Liu, X. Zhuang, M. Chen, E. Zschech, X. Feng, Efficient hydrogen production on moni4 electrocatalysts with fast water dissociation kinetics, Nat. Commun. 8 (2017), 15437, https://doi.org/10.1038/ncomms15437.
[7] Z.W. Seh, J. Kibsgaard, C.F. Dickens, I. Chorkendorff, J.K. Norskov, T.F. Jaramillo, Combining theory and experiment in electrocatalysis: insights into materials design, Science 355 (2017) 146–158, https://doi.org/10.1126/science.aad4998.
[8] D. Xiao, C. Huang, Y. Luo, K. Tang, Q. Ruan, G. Wang, P.K. Chu, Atomic-scale intercalation of graphene layers into $mose_2$ nanoflower sheets as a highly efficient catalyst for hydrogen evolution reaction, ACS Appl. Mater. Interfaces 12 (2020) 2460–2468, https://doi.org/10.1021/acsami.9b18302.
[9] L. Najafi, S. Bellani, R. Oropesa-Nuñez, A. Ansaldo, M. Prato, A.E. Del Rio Castillo, F. Bonaccorso, Doped-$mose_2$ nanoflakes/3d metal oxide-hydr(oxy) oxides hybrid catalysts for ph-universal electrochemical hydrogen evolution reaction, Adv. Energy Mater. 8 (2018), 1801764, https://doi.org/10.1002/aenm.201801764.
[10] S. Chandrasekaran, L. Yao, L. Deng, C. Bowen, Y. Zhang, S. Chen, Z. Lin, F. Peng, P. Zhang, Recent advances in metal sulfides: from controlled fabrication to electrocatalytic, photocatalytic and photoelectrochemical water splitting and beyond, Chem. Soc. Rev. 48 (2019) 4178–4280, https://doi.org/10.1039/c8cs00664d.
[11] B. Yao, J. Zhang, X. Fan, J. He, Y. Li, Surface engineering of nanomaterials for photo-electrochemical water splitting, Small 15 (2019), 1803746, https://doi.org/10.1002/smll.201803746.
[12] S. Dou, L. Tao, R. Wang, S. El Hankari, R. Chen, S. Wang, Plasma-assisted synthesis and surface modification of electrode materials for renewable energy, Adv. Mater. 30 (2018), e1705850, https://doi.org/10.1002/adma.201705850.
[13] L. Xu, Q. Jiang, Z. Xiao, X. Li, J. Huo, S. Wang, L. Dai, Plasma-engraved co_3o_4 nanosheets with oxygen vacancies and high surface area for the oxygen evolution reaction, Angew. Chem. Int. Ed. 55 (2016) 5277–5281, https://doi.org/10.1002/anie.201600687.
[14] B. Xia, T. Wang, X. Jiang, T. Zhang, J. Li, W. Xiao, P. Xi, D. Gao, D. Xue, J. Ding, Ar^{2+} beam irradiation-induced multivancancies in $MoSe_2$ nanosheet for enhanced electrochemical hydrogen evolution, ACS Energy Lett. 3 (2018) 2167–2172, https://doi.org/10.1021/acsenergylett.8b01209.
[15] D. Xiao, Q. Ruan, D.L. Bao, Y. Luo, C. Huang, S. Tang, J. Shen, C. Cheng, P.K. Chu, Effects of ion energy and density on the plasma etching-induced surface area, edge electrical field, and multivacancies in $MoSe_2$ nanosheets for enhancement of the hydrogen evolution reaction, Small 16 (2020), e2001470, https://doi.org/10.1002/smll.202001470.
[16] Y. Guo, T. Wang, J. Chen, J. Zheng, X. Li, K.K. Ostrikov, Air plasma activation of catalytic sites in a metal-cyanide framework for efficient oxygen evolution reaction, Adv. Energy Mater. 8 (2018), 1800085, https://doi.org/10.1002/aenm.201800085.
[17] D. Zhou, X. Xiong, Z. Cai, N. Han, Y. Jia, Q. Xie, X. Duan, T. Xie, X. Zheng, X. Sun, X. Duan, Flame-engraved nickel-iron layered double hydroxide nanosheets for boosting oxygen evolution reactivity, Small Methods 2 (2018), 1800083, https://doi.org/10.1002/smtd.201800083.
[18] H. Fan, W. Chen, G. Chen, J. Huang, C. Song, Y. Du, C. Li, K. Ostrikov, Plasma-heteroatom-doped ni-v-fe trimetallic phospho-nitride as high-performance

bifunctional electrocatalyst, App. Catal. B-Environ. 268 (2020), 118440, https://doi.org/10.1016/j.apcatb.2019.118440.
[19] W. Zhang, Y. Tang, L. Yu, X.-Y. Yu, Activating the alkaline hydrogen evolution performance of mo-incorporated Ni(OH)$_2$ by plasma-induced heterostructure, App. Catal. B-Environ. 260 (2020), 118154, https://doi.org/10.1016/j.apcatb.2019.118154.
[20] Q. Zhang, W. Chen, G. Chen, J. Huang, C. Song, S. Chu, R. Zhang, G. Wang, C. Li, K. K. Ostrikov, Bi-metallic nitroxide nanodot-decorated tri-metallic sulphide nanosheets by on-electrode plasma-hydrothermal sprouting for overall water splitting, App. Catal. B-Environ. 261 (2020), 118254, https://doi.org/10.1016/j.apcatb.2019.118254.
[21] A.T. Barton, L.A. Walsh, C.M. Smyth, X. Qin, R. Addou, C. Cormier, P.K. Hurley, R. M. Wallace, C.L. Hinkle, Impact of etch processes on the chemistry and surface states of the topological insulator bi$_2$se$_3$, ACS Appl. Mater. Interfaces 11 (2019) 32144–32150, https://doi.org/10.1021/acsami.9b10625.
[22] K. Chen, A. Roy, A. Rai, A. Valsaraj, X. Meng, F. He, X. Xu, L.F. Register, S. Banerjee, Y. Wang, Carrier trapping by oxygen impurities in molybdenum diselenide, ACS Appl, Mater. Interfaces 10 (2018) 1125–1131, https://doi.org/10.1021/acsami.7b15478.
[23] W. Chen, Y. Zhang, G. Chen, R. Huang, Y. Zhou, Y. Wu, Y. Hu, K. Ostrikov, Mesoporous cobalt–iron–organic frameworks: a plasma-enhanced oxygen evolution electrocatalyst, J. Mater. Chem. A 7 (2019) 3090–3100, https://doi.org/10.1039/c8ta10952d.
[24] Z. Wang, Y. Zhang, E.C. Neyts, X. Cao, X. Zhang, B.W.L. Jang, C.-J. Liu, Catalyst preparation with plasmas: how does it work? ACS Catal. 8 (2018) 2093–2110, https://doi.org/10.1021/acscatal.7b03723.
[25] J. Kibsgaard, Z. Chen, B.N. Reinecke, T.F. Jaramillo, Engineering the surface structure of mos$_2$ to preferentially expose active edge sites for electrocatalysis, Nat. Mater. 11 (2012) 963–969, https://doi.org/1.
[26] D. Kong, H. Wang, J.J. Cha, M. Pasta, K.J. Koski, J. Yao, Y. Cui, Synthesis of mos$_2$ and MoSe$_2$ films with vertically aligned layers, Nano Lett. 13 (2013) 1341–1347, https://doi.org/3.
[27] A. Derzsi, T. Lafleur, J.-P. Booth, I. Korolov, Z. Donkó, Experimental and simulation study of a capacitively coupled oxygen discharge driven by tailored voltage waveforms, Plasma Sources Sci. Technol. 25 (2016), 015004, https://doi.org/10.1088/0963-0252/25/1/015004.
[28] Y.-H. Wang, L. Wei, Y.-R. Zhang, Y.-N. Wang, Fluid simulation of inductively coupled Ar/O$_2$ plasmas: comparisons with experiment, Chin. Phys. B 24 (2015), 095203, https://doi.org/10.1088/1674-1056/24/9/095203.
[29] H.C. Kim, F. Iza, S.S. Yang, M. Radmilović-Radjenović, J.K. Lee, Particle and fluid simulations of low-temperature plasma discharges: benchmarks and kinetic effects, J. Phys. D Appl. Phys. 38 (2005) R283–R301, https://doi.org/10.1088/0022-3727/38/19/r01.
[30] Y. Jeong, Y.J. Lee, D.-C. Kwon, S.-J. Lee, J.-H. Jeon, J.H. Seo, L. Tong, H. Choe, Two-dimensional fluid simulation of large-scale, capacitively-coupled plasma discharge for display device processes, J. Nanosci. Nanotechnol. 17 (2017) 8411–8417, https://doi.org/10.1166/jnn.2017.15167.
[31] Https://lammps.Sandia.Gov/.
[32] K. Mizotani, M. Isobe, M. Fukasawa, K. Nagahata, T. Tatsumi, S. Hamaguchi, Molecular dynamics simulation of silicon oxidation enhanced by energetic hydrogen ion irradiation, J. Phys. D Appl. Phys. 48 (2015), 152002, https://doi.org/10.1088/0022-3727/48/15/152002.
[33] J.-W. Jiang, H.S. Park, T. Rabczuk, Molecular dynamics simulations of single-layer molybdenum disulphide (mos$_2$): stillinger-weber parametrization, mechanical properties, and thermal conductivity, J. Appl. Phys. 114 (2013), 064307, https://doi.org/10.1063/1.4818414.
[34] G. Kresse, J. Furthmuller, Efficient iterative schemes for ab initio total-energy calculations using a plane-wave basis set, Phys. Rev. B 54 (1996) 11169.
[35] G. Kresse, J. Furthmuller, Efficiency of ab-initio total energy calculations for metals and semiconductors using a plane-wave basis set, Comp. Mater. Sci. 6 (1996) 15–50.
[36] D. Vanderbilt, Soft self-consistent pseudopotentials in a generalized eigenvalue formalism, Phys. Rev., B Condens. Matter 41 (1990) 7892–7895, https://doi.org/10.1103/physrevb.41.7892.
[37] J.A. Stefan Grimme, Stephan Ehrlich, Helge Krieg, A consistent and accurate ab initio parametrization of density functional dispersion correction (dft-d) for the 94 elements h-pu, J. Chem. Phys. 132 (2010) 1–18, https://doi.org/10.1063/1.3382344.
[38] J.K. Nørskov, T. Bligaard, A. Logadottir, J.R. Kitchin, J.G. Chen, S. Pandelov, U. Stimming, Trends in the exchange current for hydrogen evolution, J. Electrochem. Soc. 152 (2005) J23, https://doi.org/10.1149/1.1856988.
[39] X. Zhang, X. Zeng, M. Yang, Y. Qi, Investigation of a branchlike moo$_3$ /polypyrrole hybrid with enhanced electrochemical performance used as an electrode in supercapacitors, ACS Appl. Mater. Interfaces 6 (2014) 1125–1130, https://doi.org/10.1021/am404724u.
[40] A. Khademi, R. Azimirad, A.A. Zavarian, A.Z. Moshfegh, Growth and field emission study of molybdenum oxide nanostars, J. Phys. Chem. C 113 (2009) 19298–19304, https://doi.org/10.1021/jp9056237.
[41] H.S. Kim, J.B. Cook, H. Lin, J.S. Ko, S.H. Tolbert, V. Ozolins, B. Dunn, Oxygen vacancies enhance pseudocapacitive charge storage properties of MoO3-x, Nat. Mater. 16 (2017) 454–460, https://doi.org/10.1038/nmat4810.
[42] C. Zhang, L. Jiang, Y. Zhang, J. Hu, M.K.H. Leung, Janus effect of o$_2$ plasma modification on the electrocatalytic hydrogen evolution reaction of MoS$_2$, J. Catal. 361 (2018) 384–392, https://doi.org/10.1016/j.jcat.2018.03.018.
[43] S.H. Song, B.H. Kim, D.H. Choe, J. Kim, D.C. Kim, D.J. Lee, J.M. Kim, K.J. Chang, S. Jeon, Bandgap widening of phase quilted, 2d mos$_2$ by oxidative intercalation, Adv. Mater. 27 (2015) 3152–3158, https://doi.org/10.1002/adma.201500649.
[44] J. Jadwiszczak, C. O'callaghan, Y. Zhou, Etc., Oxide-mediated recovery of field-effect mobilit in plasma-treated mos$_2$, Sci. Adv. 4 (2018), eaao5031, https://doi.org/10.1126/sciadv.aao5031.
[45] T.Y. Ko, A. Jeong, W. Kim, J. Lee, Y. Kim, J.E. Lee, G.H. Ryu, K. Park, D. Kim, Z. Lee, M.H. Lee, C. Lee, S. Ryu, On-stack two-dimensional conversion of MoS$_2$ into moo$_3$, 2D Mater. 4 (2016), 014003, https://doi.org/10.1088/2053-1583/4/1/014003.
[46] R. Razaq, D. Sun, Y. Xin, Q. Li, T. Huang, Z. Zhang, Y. Huang, Nanoparticle assembled mesoporous MoO$_2$ microrods derived from metal organic framework and wrapped with graphene as the sulfur host for long-life lithium-sulfur batteries, Adv. Mater. Interfaces 6 (2019), 1801636, https://doi.org/10.1002/admi.201801636.
[47] J.M.A. Thøgersen, L. Vines, M.F. Sunding, A. Olsen, S. Diplas, M. Mitome, Y. Bando, Composition and structure of pd nanoclusters in siox thin film, J. Appl. Phys. 109 (2011), 084329, https://doi.org/10.1063/1.3561492.
[48] M.H. Hendrik Bluhm, Axel Knop-Gericke, Evgueni Kleimenov, Robert Schlögl, Detre Teschner, Valerii I. Bukhtiyarov, D. Frank Ogletree, Miquel Salmeron, Methanol oxidation on a copper catalyst investigated using in situ x-ray photoelectron spectroscopy, J. Phys. Chem. B 108 (2004) 14340–14347, https://doi.org/10.1021/jp040080j.
[49] A. Chen, K. Zhu, H. Zhong, Q. Shao, G. Ge, A new investigation of oxygen flow influence on ito thin films by magnetron sputtering, Sol. Energy Mater. Sol. Cells 120 (2014) 157–162, https://doi.org/10.1016/j.solmat.2013.08.036.
[50] P. Jiang, Y. Yang, R. Shi, G. Xia, J. Chen, J. Su, Q. Chen, Pt-like electrocatalytic behavior of Ru– MoO$_2$ nanocomposites for the hydrogen evolution reaction, J. Mater. Chem. A Mater. Energy Sustain. 5 (2017) 5475–5485, https://doi.org/10.1039/c6ta09994g.
[51] Y. Jin, P.K. Shen, Nanoflower-like metallic conductive MoO$_2$ as a high-performance non-precious metal electrocatalyst for the hydrogen evolution reaction, J. Mater. Chem. A 3 (2015) 20080–20085, https://doi.org/10.1039/c5ta06018d.
[52] Da.C.J.R. Shallenberger, S.W. Novak, R.L. Moore, Oxide thickness determination by xps, aes, sims, rbs and tem. 1998 International Conference on Ion Implantation Technology. Proceedings 1, 1999, pp. 79–82, https://doi.org/10.1109/IIT.1999.812056.
[53] S. Robertson, Sheaths in laboratory and space plasmas, Plasma Phys. Control. Fusion 55 (2013), 093001, https://doi.org/10.1088/0741-3335/55/9/093001.
[54] D.J. Economou, Hybrid simulation of low temperature plasmas: a brief tutorial, Plasma Process. Polym. 14 (2017), 1600152, https://doi.org/10.1002/ppap.201600152.
[55] S. Huang, C. Huard, S. Shim, S.K. Nam, I.-C. Song, S. Lu, M.J. Kushner, Plasma etching of high aspect ratio features in sio$_2$ using ar/c$_4$f$_8$/o$_2$ mixtures: a computational investigation, J. Vac. Sci. Technol. A 37 (2019), 031304, https://doi.org/10.1116/1.5090606.
[56] V. Martirosyan, O. Joubert, E. Despiau-Pujo, Modification mechanisms of silicon thin films in low-temperature hydrogen plasmas, J. Phys. D Appl. Phys. 52 (2019), 055204, https://doi.org/10.1088/1361-6463/aaefe0.
[57] L. Tao, X. Duan, C. Wang, X. Duan, S. Wang, Plasma-engineered MoS$_2$ thin-film as an efficient electrocatalyst for hydrogen evolution reaction, Chem. Commun. 51 (2015) 7470–7473, https://doi.org/10.1039/c5cc01981h.
[58] J. Zhang, Y. Chen, M. Liu, K. Du, Y. Zhou, Y. Li, Z. Wang, J. Zhang, 1T@2H- MoSe$_2$ nanosheets directly arrayed on ti plate: an efficient electrocatalytic electrode for hydrogen evolution reaction, Nano Res. 11 (2018) 4587–4598, https://doi.org/10.1007/s12274-018-2040-x.
[59] J. Zhang, J. Qian, J. Ran, P. Xi, L. Yang, D. Gao, Engineering lower coordination atoms onto NiO/Co$_3$O$_4$ heterointerfaces for boosting oxygen evolution reactions, ACS Catal. 10 (2020) 12376–12384, https://doi.org/10.1021/acscatal.0c03756.
[60] J. Zhang, T. Wang, D. Xue, C. Guan, P. Xi, D. Gao, W. Huang, Energy-level engineered hollow n-doped NiS$_{1.03}$ for Zn–air batteries, Energy Storage Mater. 25 (2020) 202–209, https://doi.org/10.1016/j.ensm.2019.10.014.
[61] S. Barja, S. Refaely-Abramson, B. Schuler, D.Y. Qiu, A. Pulkin, S. Wickenburg, H. Ryu, M.M. Ugeda, C. Kastl, C. Chen, C. Hwang, A. Schwartzberg, S. Aloni, S. K. Mo, D. Frank Ogletree, M.F. Crommie, O.V. Yazyev, S.G. Louie, J.B. Neaton, A. Weber-Bargioni, Identifying substitutional oxygen as a prolific point defect in monolayer transition metal dichalcogenides, Nat. Commun. 10 (2019), 3382, https://doi.org/10.1038/s41467-019-11342-2.
[62] J. Peto, T. Ollar, P. Vancso, Z.I. Popov, G.Z. Magda, G. Dobrik, C. Hwang, P. B. Sorokin, L. Tapaszto, Spontaneous doping of the basal plane of MoS$_2$ single layers through oxygen substitution under ambient conditions, Nat. Chem. 10 (2018) 1246–1251, https://doi.org/10.1038/s41557-018-0136-2.
[63] Q. Liang, Q. Zhang, J. Gou, T. Song, H. Arramel, M. Chen, S.X. Yang, Q. Lim, R. Wang, N. Zhu, S.C. Yakovlev, W. Tan, K.S. Zhang, A.T.S. Novoselov, Wee, Performance improvement by ozone treatment of 2d PdSe$_2$, ACS Nano 14 (2020) 5668–5677, https://doi.org/10.1021/acsnano.0c00180.

Supporting Information

Experimental and theoretical investigation of the control and balance of active sites on oxygen plasma-functionalized $MoSe_2$ nanosheets for efficient hydrogen evolution reaction

Dezhi Xiao [a], De-Liang Bao [b, c], Xiongyi Liang [a], Ying Wang [a], Jie Shen [d], Cheng Cheng [d], Paul K. Chu [a*]

[a] Department of Physics, Department of Materials Science and Engineering, and Department of Biomedical Engineering, City University of Hong Kong, Tat Chee Avenue, Kowloon, Hong Kong, China

[b] Department of Physics and Astronomy, Vanderbilt University, Nashville, Tennessee 37235, USA

[c] Institute of Physics and University of the Chinese Academy of Sciences, Chinese Academy of Sciences, Beijing 100190, China

[d] Institute of Plasma Physics, Chinese Academy of Sciences, Hefei 230031, China

* Corresponding author: P. K. Chu (paul.chu@cityu.edu.hk)

Table S1. XPS analysis of different Mo valence states.

Samples	Mo^{4+} $3d_{3/2}$	Mo^{4+} $3d_{5/2}$	Mo^{6+} $3d_{3/2}$	Mo^{6+} $3d_{5/2}$	Mo^{6+} (%)
0W	28666.64	45539.317	0	0	0
20W	14332.97	29882.18	1705.645	7366.214	17.02
30W	11038.47	28353.509	2685.786	10135.03	24.56

Table S2. Reactions in the oxygen discharge for simulation.

Excitation	Ionization	Dissociation	Collision and Reactions
$e+O_2(V=0)\rightarrow e+O_2(V=1...7)$	$e+O_2\rightarrow 2e+O_2^+$	$e+O_2\rightarrow e+2O$	$e+2O_2\rightarrow O_2^-+O_2$
$e+O_2\rightarrow e+O_2a1d$	$e+O_2a1d\rightarrow 2e+O_2^+$	$e+O_2\rightarrow e+O+O1s$	$O_2+O_2a1d\rightarrow 2O_2$
$e+O_2\rightarrow e+O_2b1s$	$e+O_2b1s\rightarrow 2e+O_2^+$	$e+O_2\rightarrow e+O+O1d$	$O_2+O_2b1s\rightarrow 2O_2$
$e+O_2\rightarrow e+O_2245$	$e+O_2245\rightarrow 2e+O_2^+$	$e+O_2a1d\rightarrow e+2O$	$O+O_2b1s\rightarrow O_2+O$
$e+O\rightarrow e+O$	$e+O\rightarrow 2e+O^+$	$e+O_2b1s\rightarrow e+2O$	$O+O_2a1d\rightarrow O_2+O$
$e+O\rightarrow e+O1s$	$e+O1s\rightarrow 2e+O^+$	$e+O_2245\rightarrow e+2O$	$O_2+O_2245\rightarrow 2O_2$
$e+O\rightarrow e+O1d$	$e+O1d\rightarrow 2e+O^+$	$e+O_2\rightarrow O+O^-$ (e attachment)	$O_2+O1d\rightarrow O+O_2$
		$e+O_2^+\rightarrow e+2O$	$O_2+O1s\rightarrow O+O_2$
		$e+O_2^+\rightarrow O+O1d$	$O+O1s\rightarrow 2O$
		$e+O_2^+\rightarrow O+O1s$	$O+O1d\rightarrow 2O$
			$2O+O_2\rightarrow 2O_2$
			$3O\rightarrow 2O_2+O$
			$O^++O_2\rightarrow O_2^++O$
			$O^-+O_2\rightarrow O_2^-+O$
			$O^-+O\rightarrow O_2+e$
			$O^-+O^+\rightarrow 2O$
			$O^-+O_2^+\rightarrow 3O$
			$O_2^-+O_2^+\rightarrow 2O_2$

Table S3. Comparison of the HER characteristics of plasma-treated molybdenum-based materials.

Catalysts	Electrolytes	Overpotentials (mV) (10 mA cm^{-1})	Tafel slopes (mV dec^{-1})	Refs.
$O_{2plasma}$ doped $MoSe_2$	0.5 M H_2SO_4	165	55.2	This work
$O_{2plasma}$ modified MoS_2	0.5 M H_2SO_4	131	69	[1]
$O_{2plasma}$ modified MoS_2	0.5 M H_2SO_4	550	138	[2]
$Water_{plasma}$ modified MoS_2	0.5 M H_2SO_4	164	71	[3]
$H_{2plasma}$ modified MoS_2	0.5 M H_2SO_4	193	94	[4]
$H_{2plasma}$ modified MoS_2	0.5 M H_2SO_4	183	77.6	[5]
Ar^+ etching $MoSe_2$	0.5 M H_2SO_4	148	51.6	[6]
Ar^+ irradiation $MoSe_2$	0.5 M H_2SO_4	135	35	[7]
$Ar+H_{2plasma}$ modified MoS_2	0.5 M H_2SO_4	420	86.6	[8]
H_2S_{plasma} deposited MoS_2	0.5 M H_2SO_4	394	122	[9]

Table S4. ΔG_H at the Mo, Se and O sites.

Samples	ΔG_H/eV (Mo site)	ΔG_H/eV (Se site)	ΔG_H/eV (O site)
Pristine	2.18	1.92	
O	2.05	1.86	1.05
2O	2.05	1.88	1.01
Vse (side)+O doping	-0.194	1.59	0.67
Vse (bottom)+O doping	-0.059	1.59	0.7

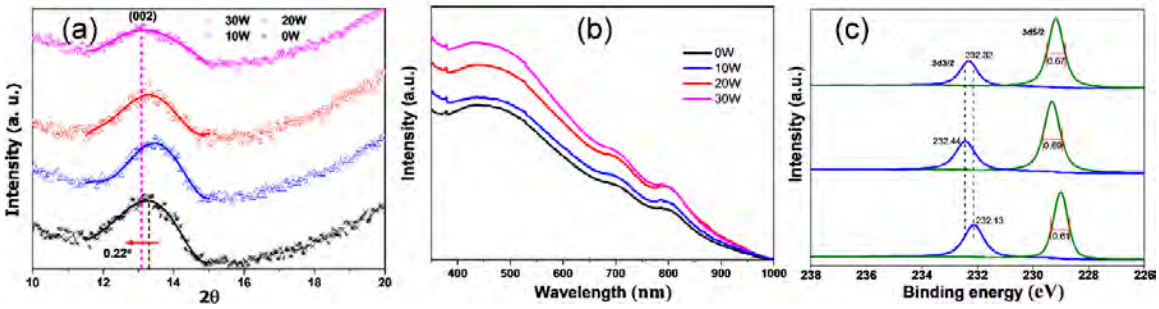

Figure S1. (a) XRD shifts of the $MoSe_2$ nanosheets processed with different power, (b) UV-vis spectra of the samples treated with different power, and (c) XPS shifts of the $MoSe_2$ nanosheets treated with different power.

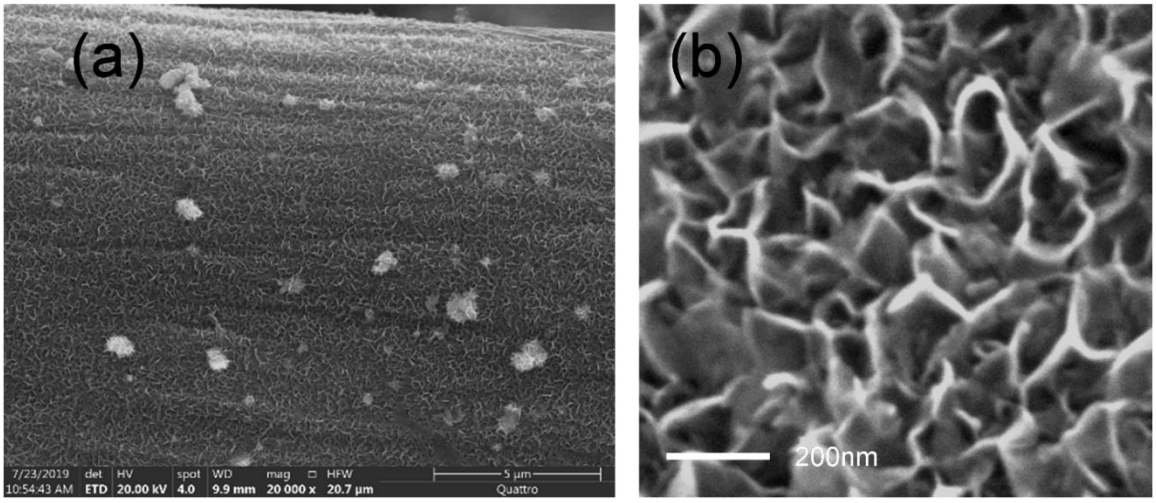

Figure S2. (a) $MoSe_2$ nanosheets synthesized on carbon felt and (b) $MoSe_2$ nanosheets modified with the 30 W oxygen plasma.

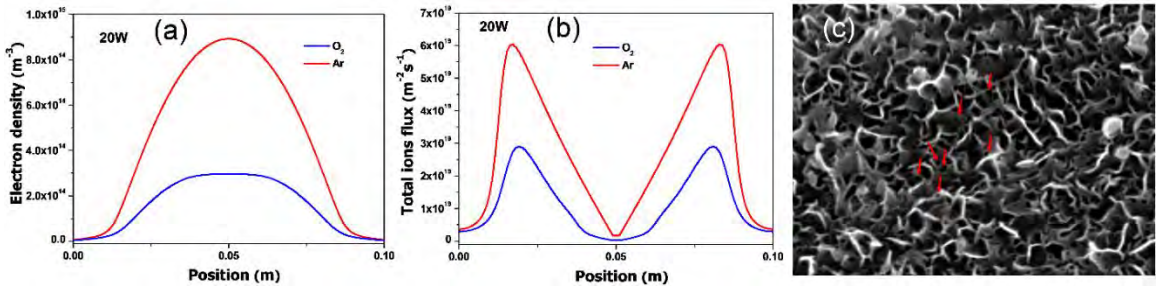

Figure S3. (a) Electron density distributions of the 20 W oxygen and argon plasmas, (b) Ion flux distributions of the 20 W oxygen and argon plasmas, and (c) SEM image of the argon plasma-etched $MoSe_2$ nanosheets using a power of 20 W.

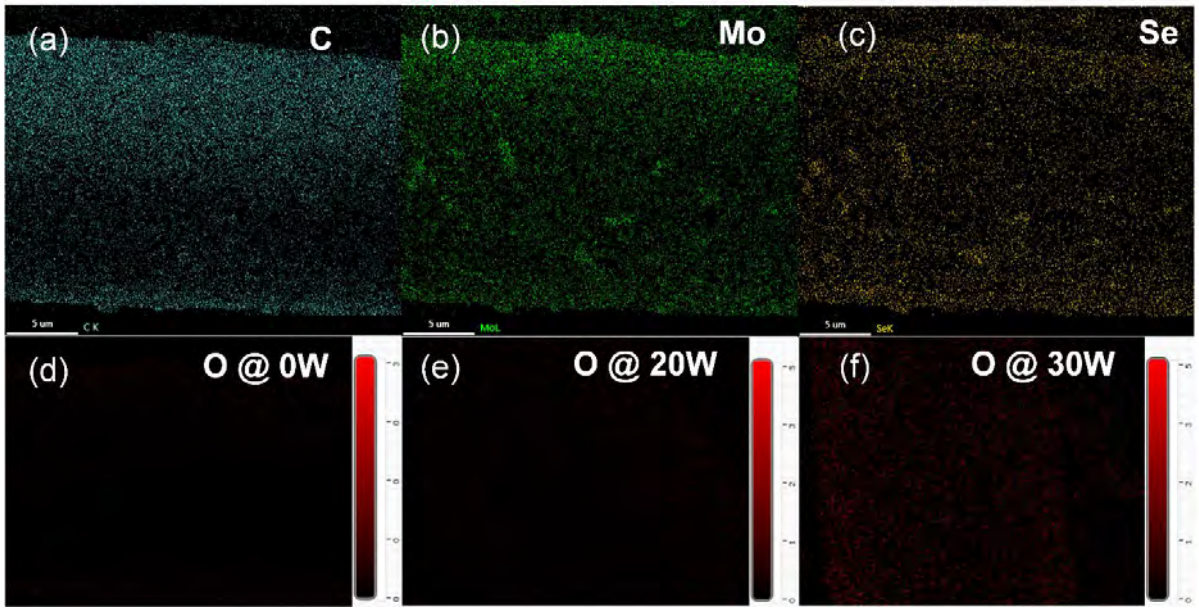

Figure S4. EDS elemental maps: (a) C, (b) Mo, and (c) Se; O: (d) 0 W, (e) 20 W, (f) 30 W.

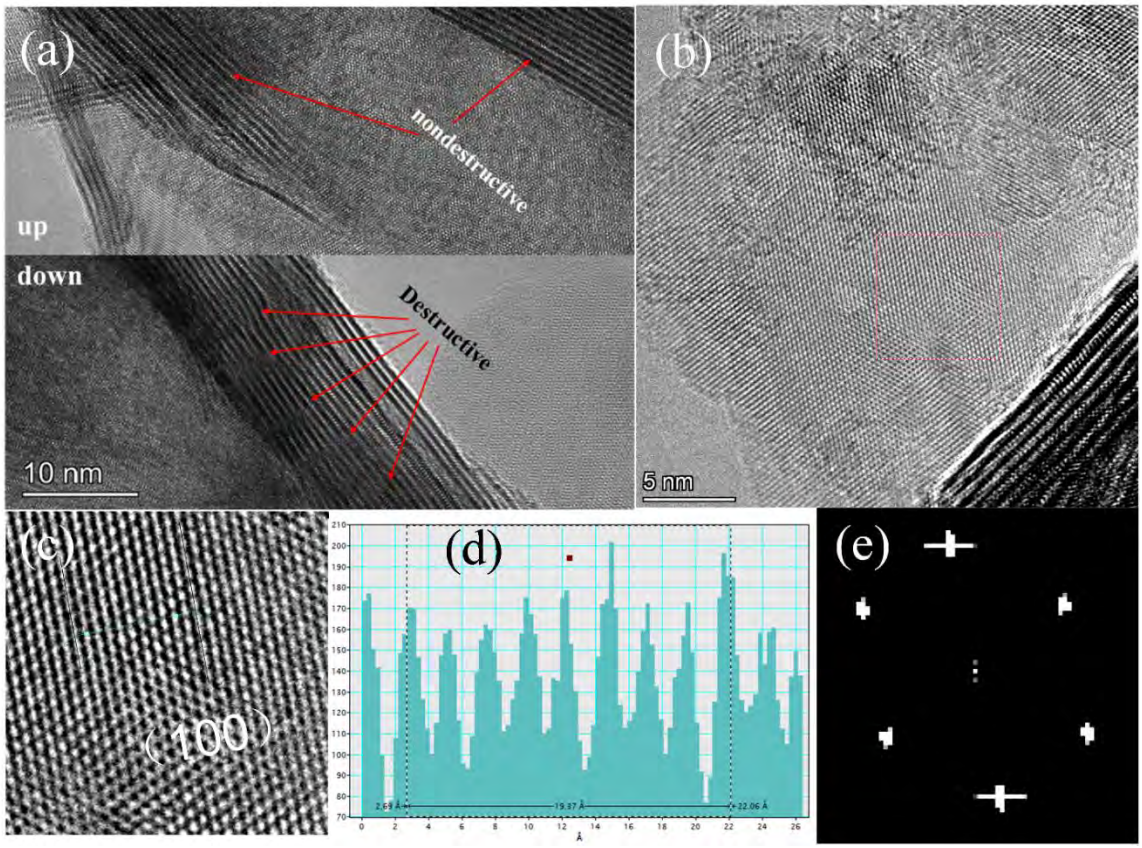

Figure S5. (a) TEM images of $MoSe_2$ treated using 0 W (top) and 20 W (bottom), (b and c) High-resolution TEM images of $MoSe_2$ treated with a power of 20 W indicating MoO_2 formation, (d) Lattice spacing distribution of the structure shown in (c), and (e) FFT image of the crystal shown in (c).

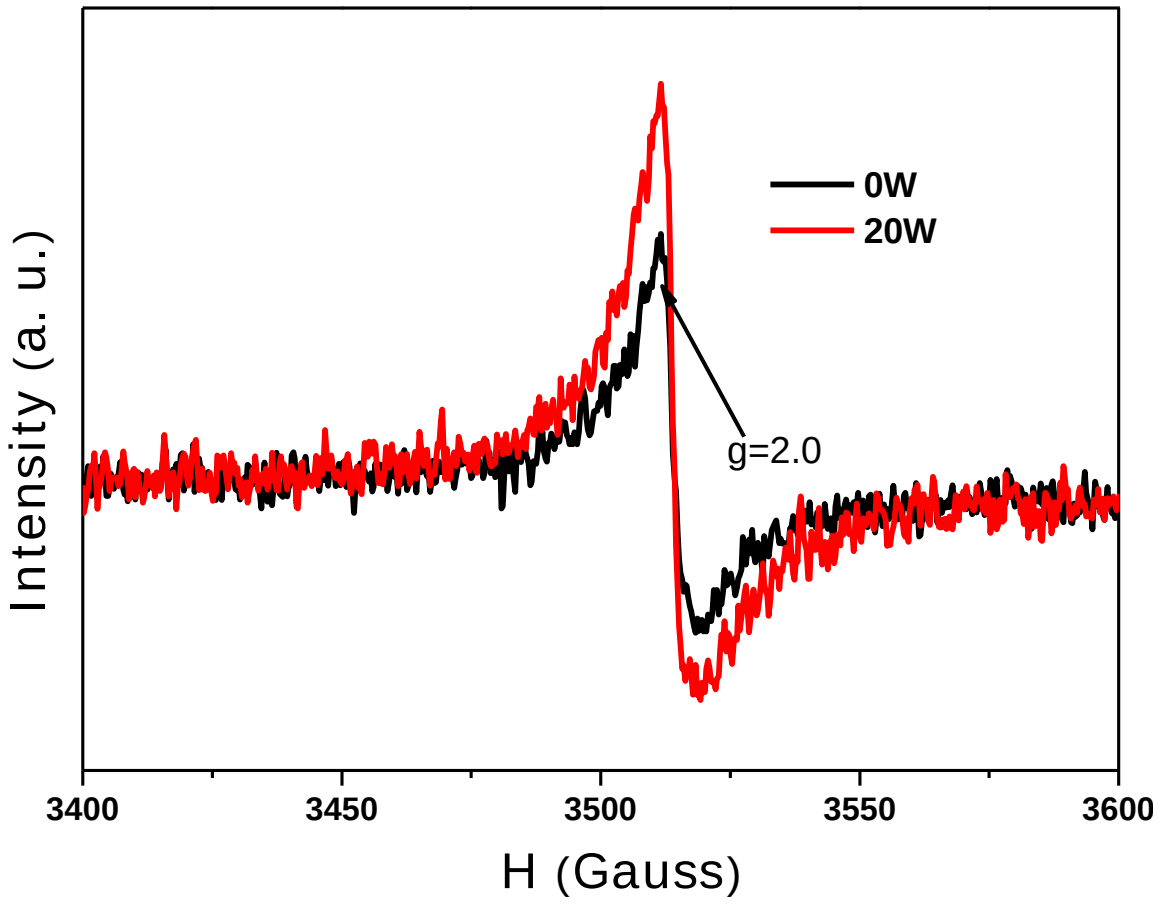

Figure S6. Electron paramagnetic resonance (EPR) measurements.

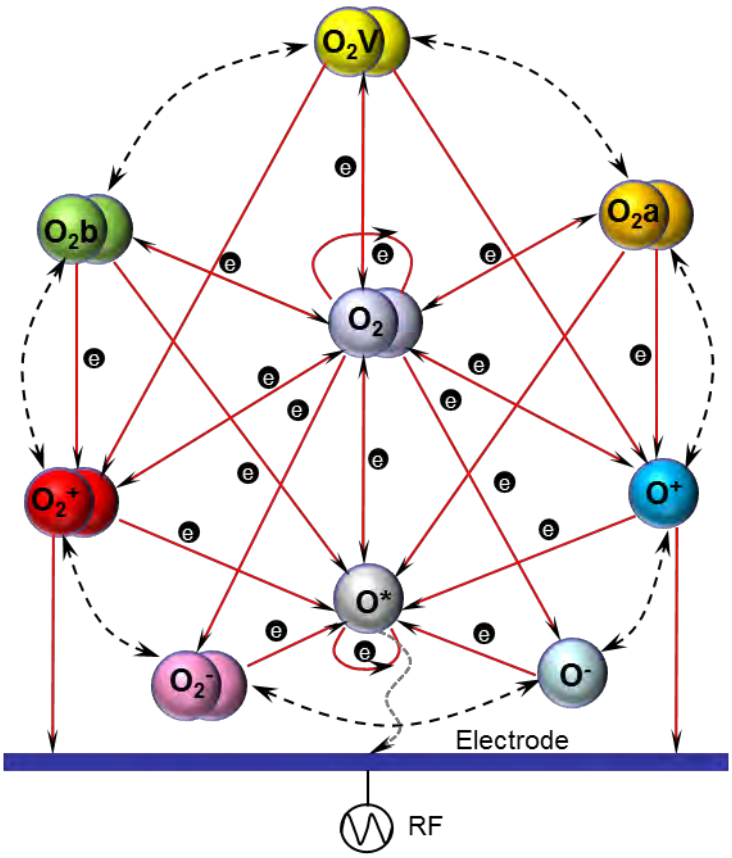

Figure S7. Illustration of the elementary processes in the oxygen plasma discharge.

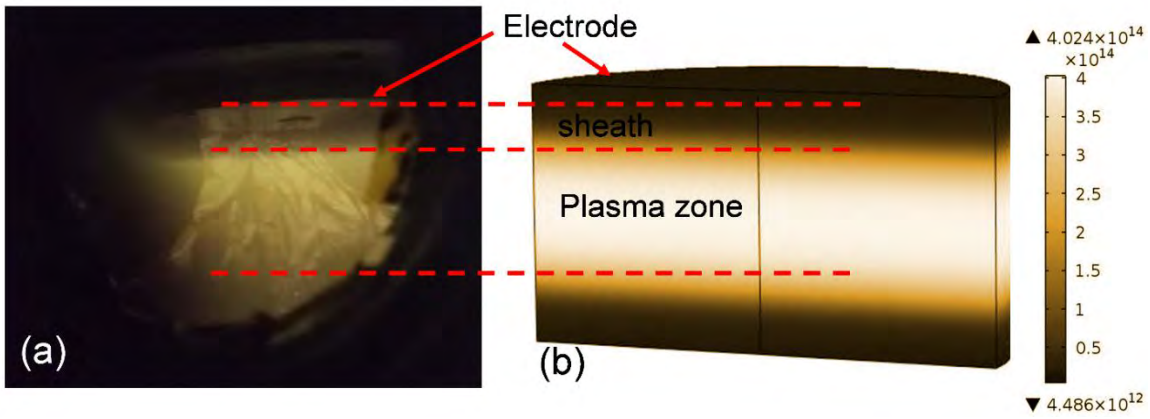

Figure S8. (a) Picture of the CCP oxygen plasma discharge and (b) Simulation results of the CCP oxygen plasma for the reactions shown in Table S2.

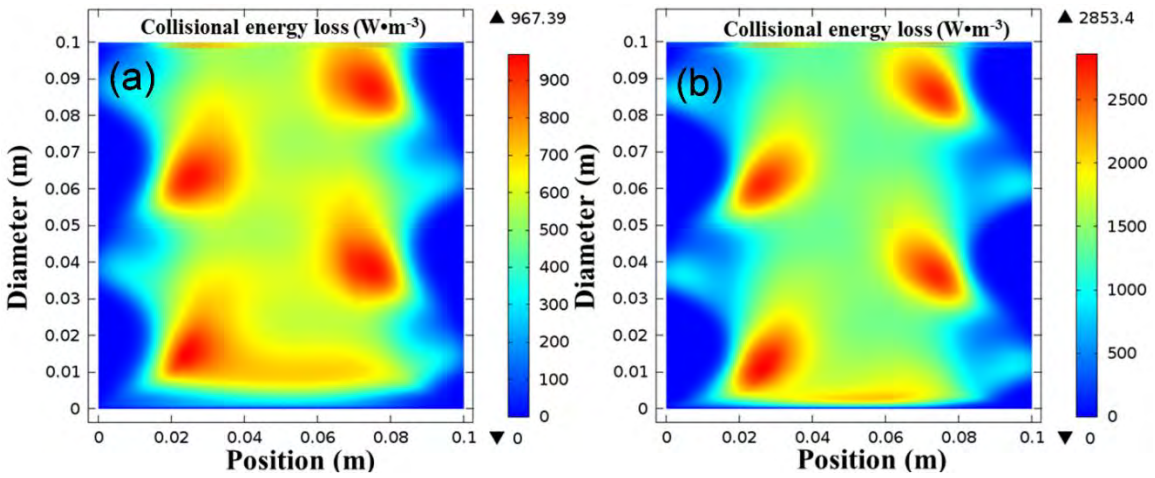

Figure S9. Collisional energy losses companied by migration of ions and radicals of the samples processed using (a) 10 W and (b) 30 W.

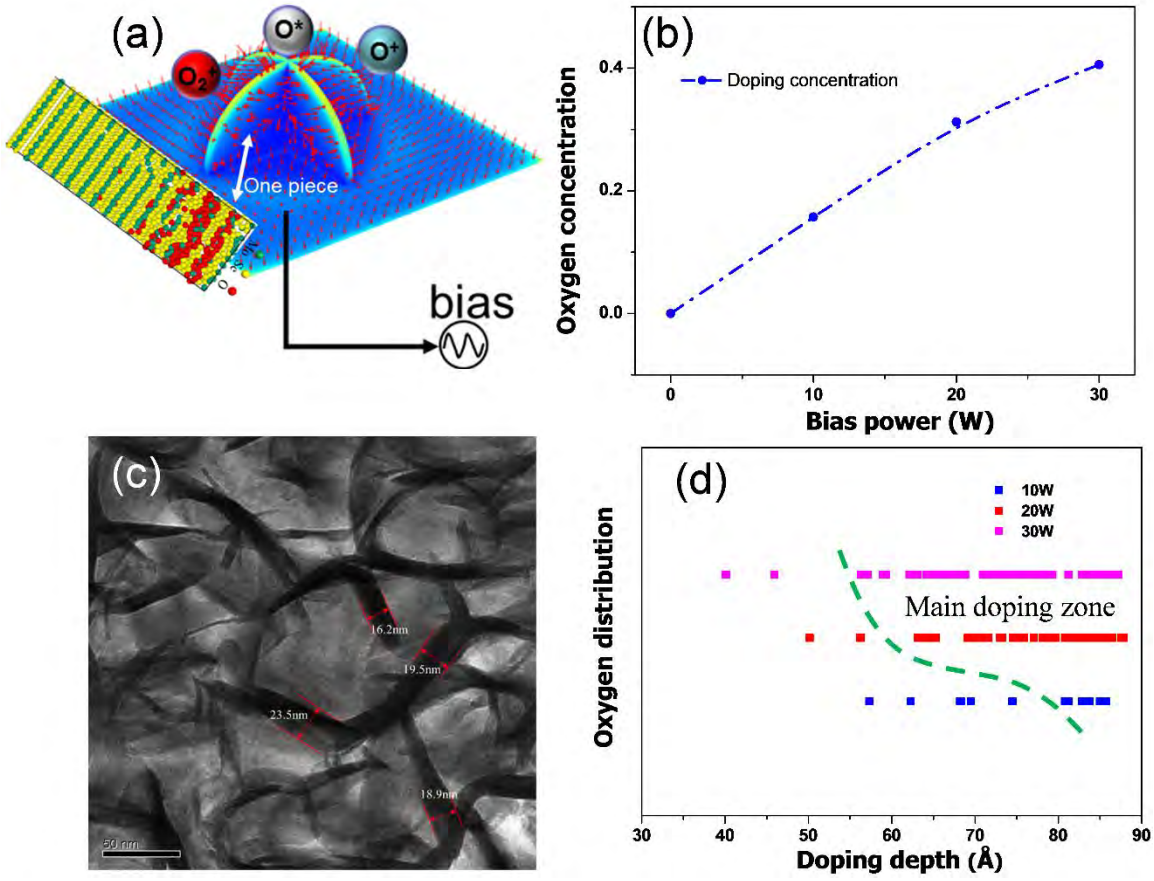

Figure S10. (a) Oxygen implantation into the $MoSe_2$ nanosheets under an electric field generated by the bias voltage, (b) Oxygen concentration derived from MD calculation, (c) TEM image showing the $MoSe_2$ nanosheet thickness, and (d) Oxygen distribution as a function of depth.

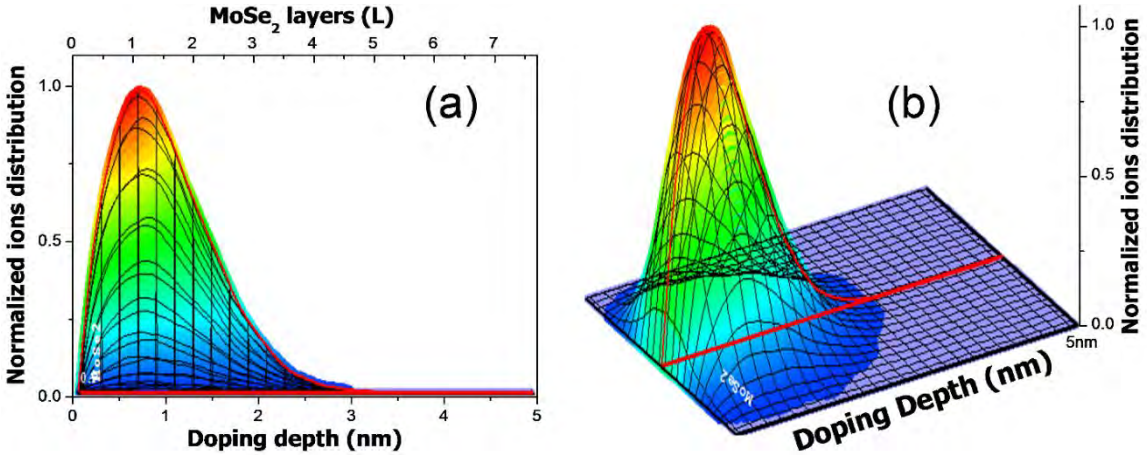

Figure S11. Oxygen distributions calculated by the Monte Carlo code: (a) 2D and (b) 3D.

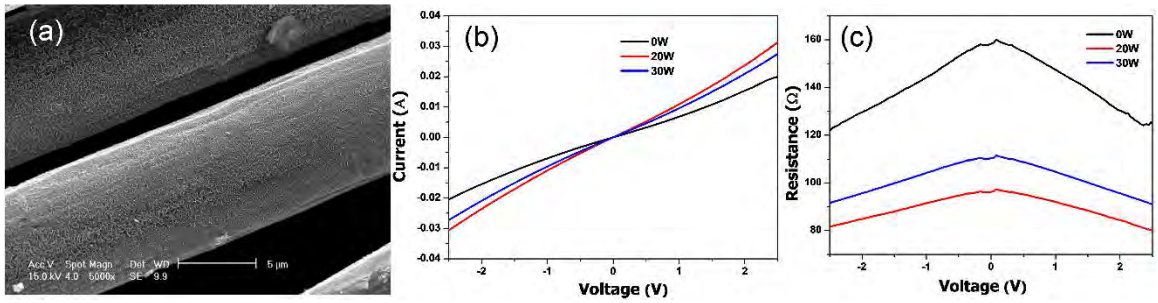

Figure S12. (a) Carbon fiber image, (b) I-V measurement, and (c) Resistance derived from I-V measurements.

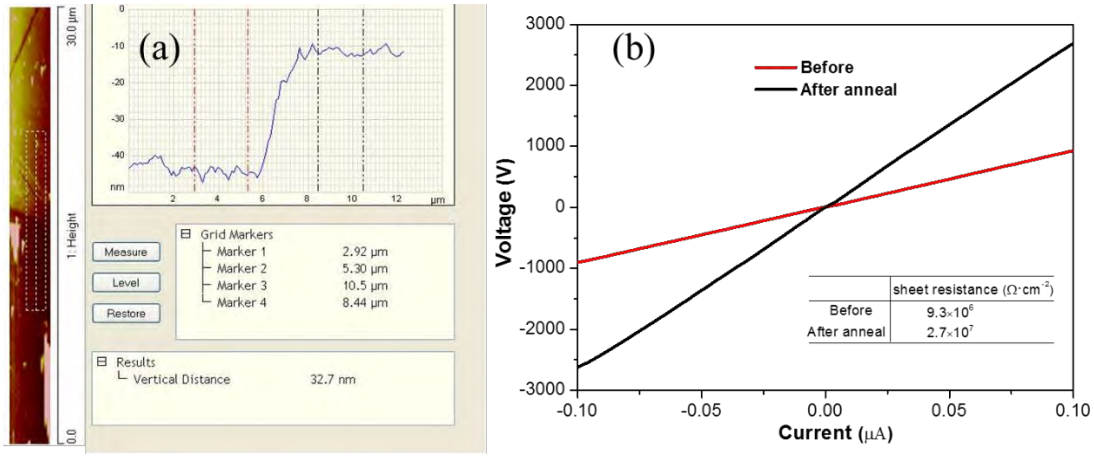

Figure S13. (a) Thickness of the $MoSe_2$ film determined by AFM and (b) I-V measurement.

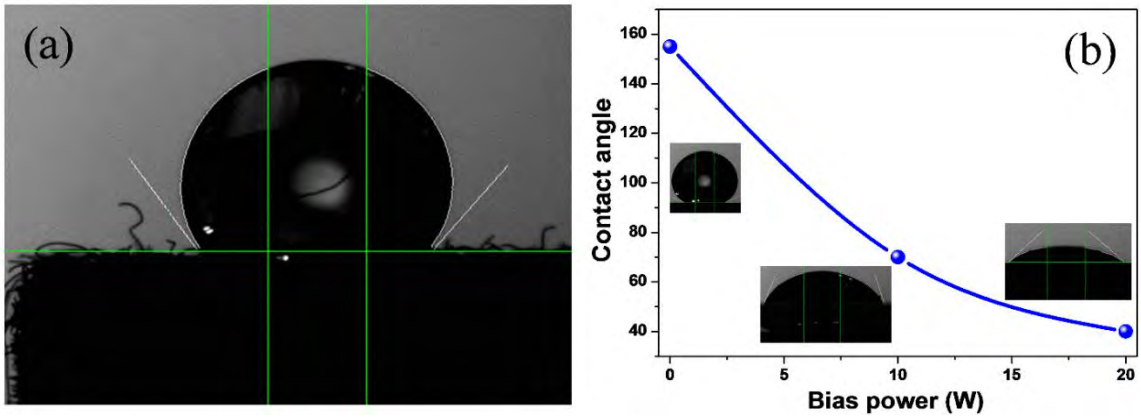

Figure S14. (a) Hydrophobic pristine $MoSe_2$ and (b) Changes in the contact angles after 10 W and 20 W plasma treatments.

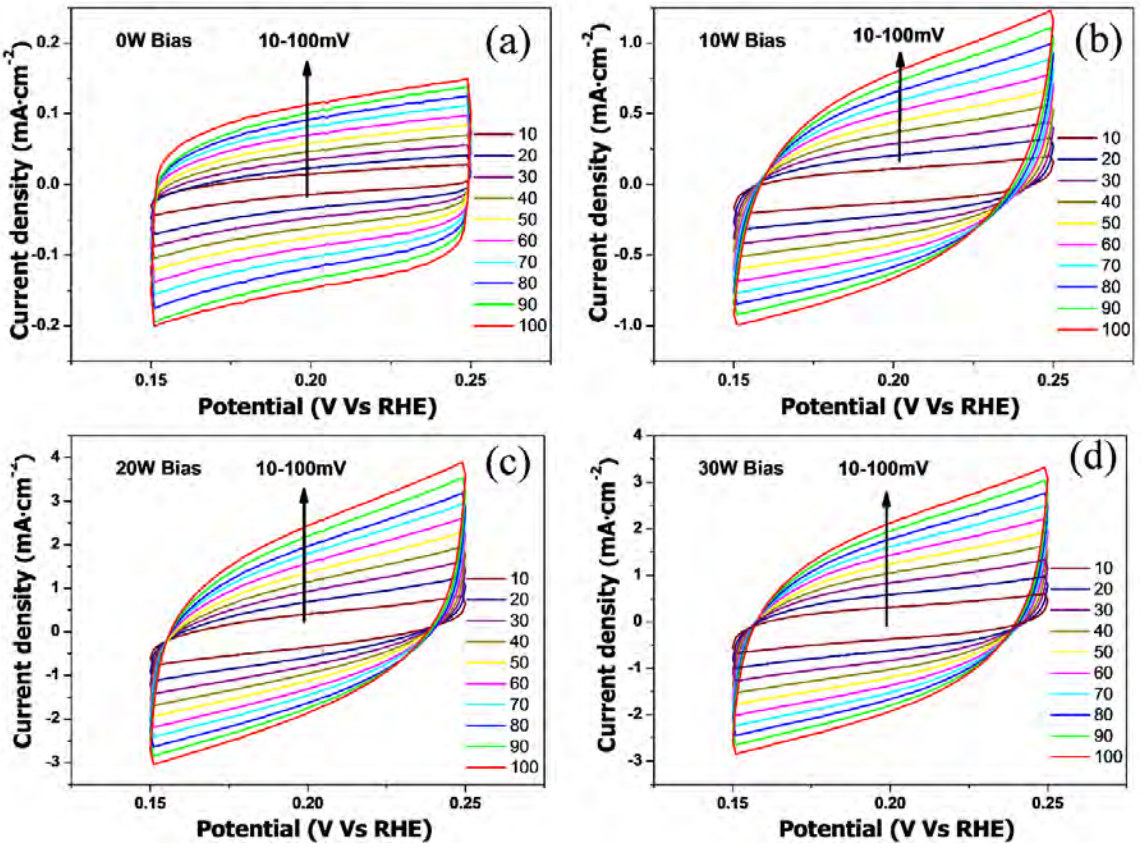

Figure S15. CV curves of the $MoSe_2$ nanosheets on carbon felt after plasma treatment using different power: (a) 0 W, (b) 10 W, (c) 20 W, and (d) 30 W.

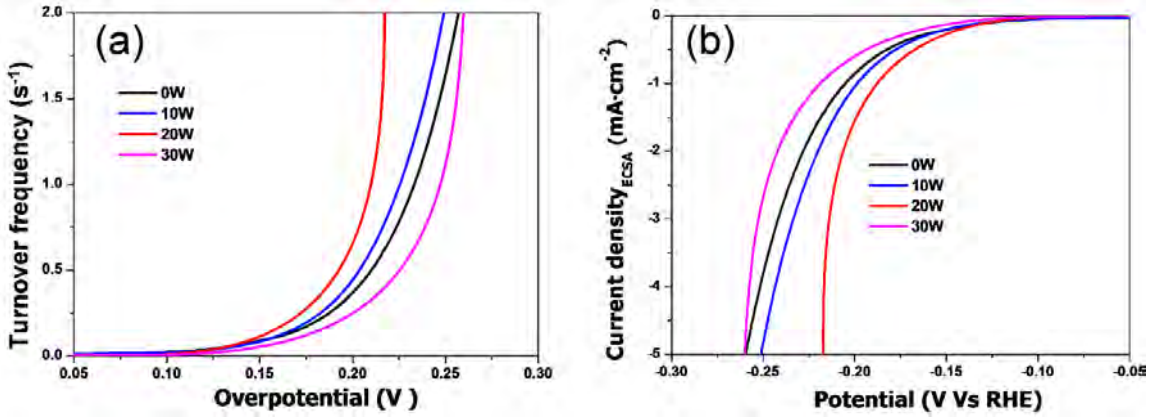

Figure S16. (a) TOFs of $MoSe_2$ treated using different discharge power and (b) LSV curves normalized by the electrochemically active area (ECSA).

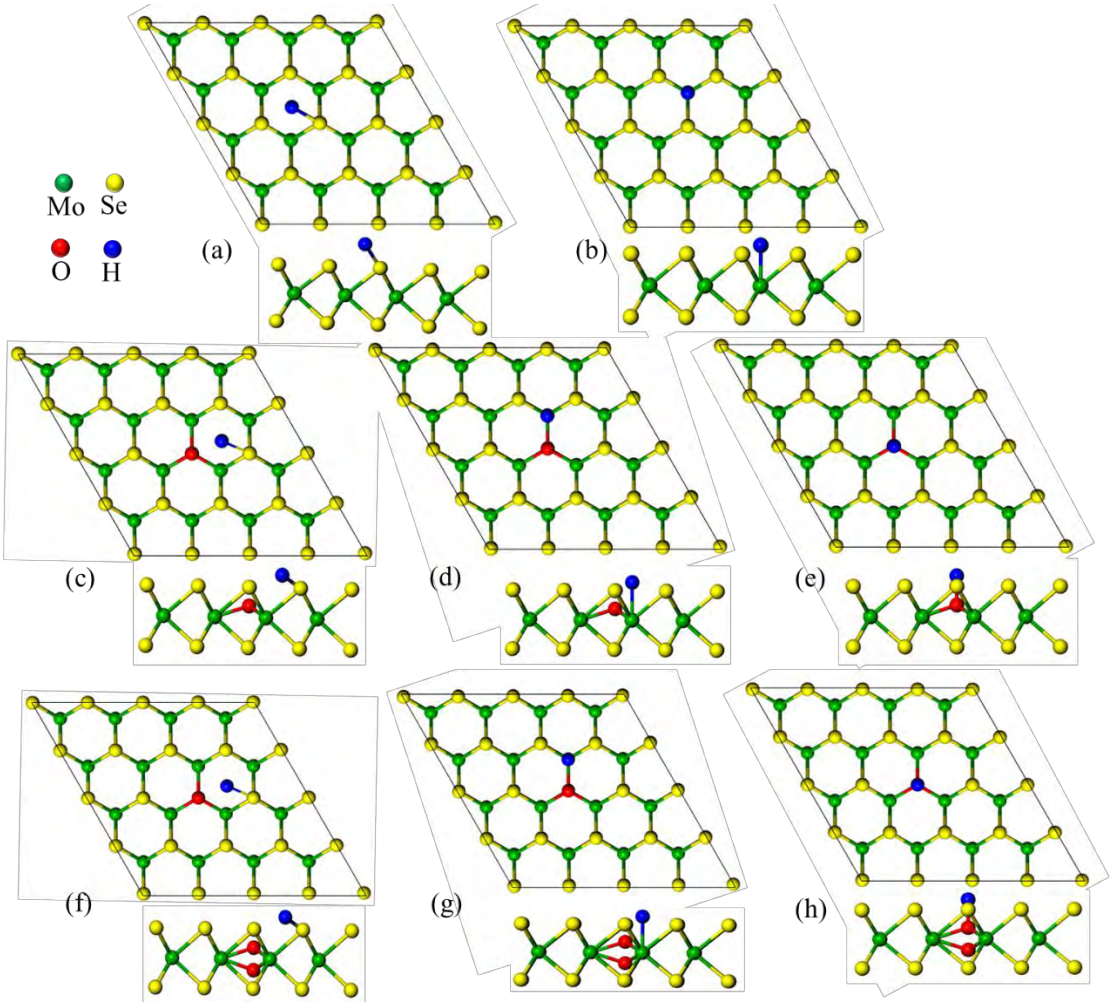

Figure S17. Hydrogen absorption on different active sites of the pristine $MoSe_2$ and surfaces doped with one oxygen atom and two oxygen atoms: (a, c, and e) Mo site, (b, d, and g) Se site, and (e and h) O site.

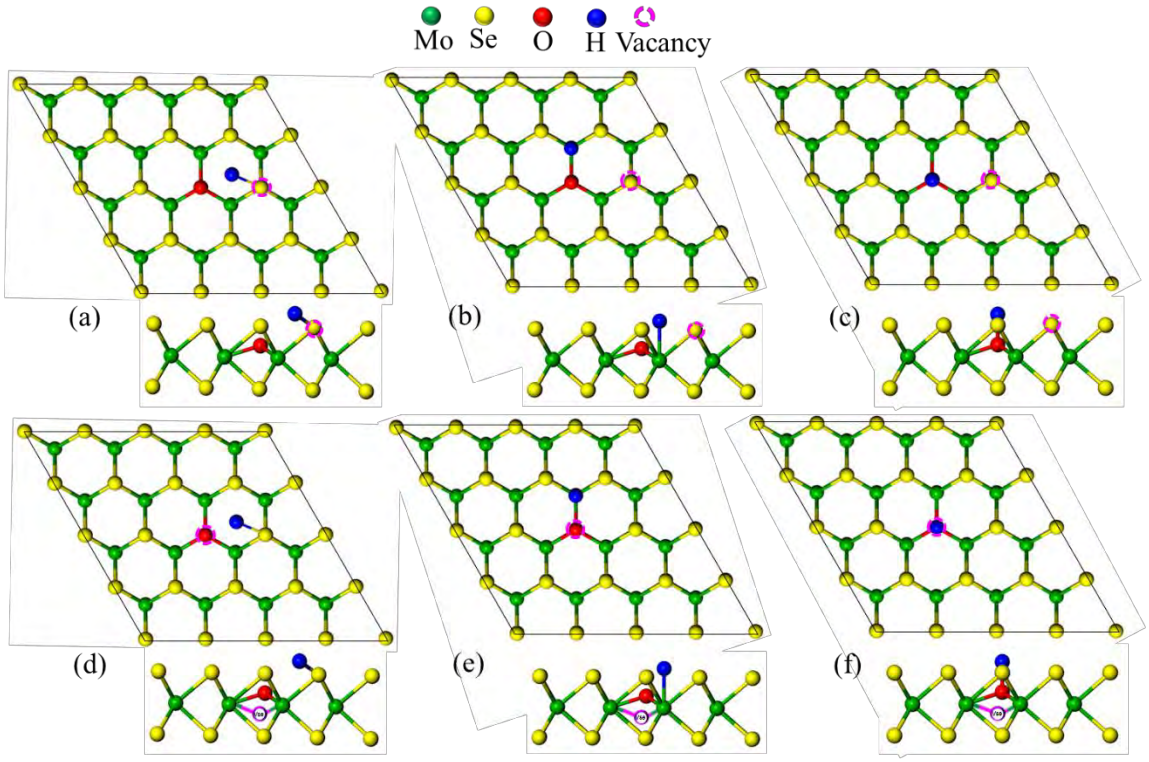

Figure S18. Hydrogen absorption on different active sites of surfaces doped with one oxygen atom and one Se vacancy (side and bottom of O): (a, and d) Mo site, (b, and e) Se site, and (c and f) O site.

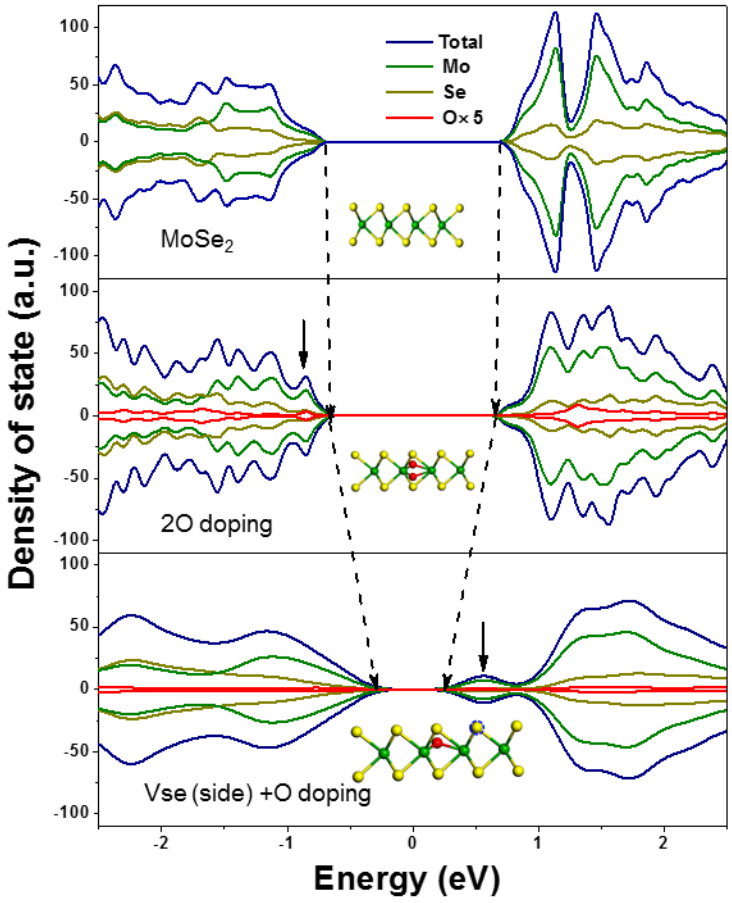

Figure S19. DOS distributions in different cases

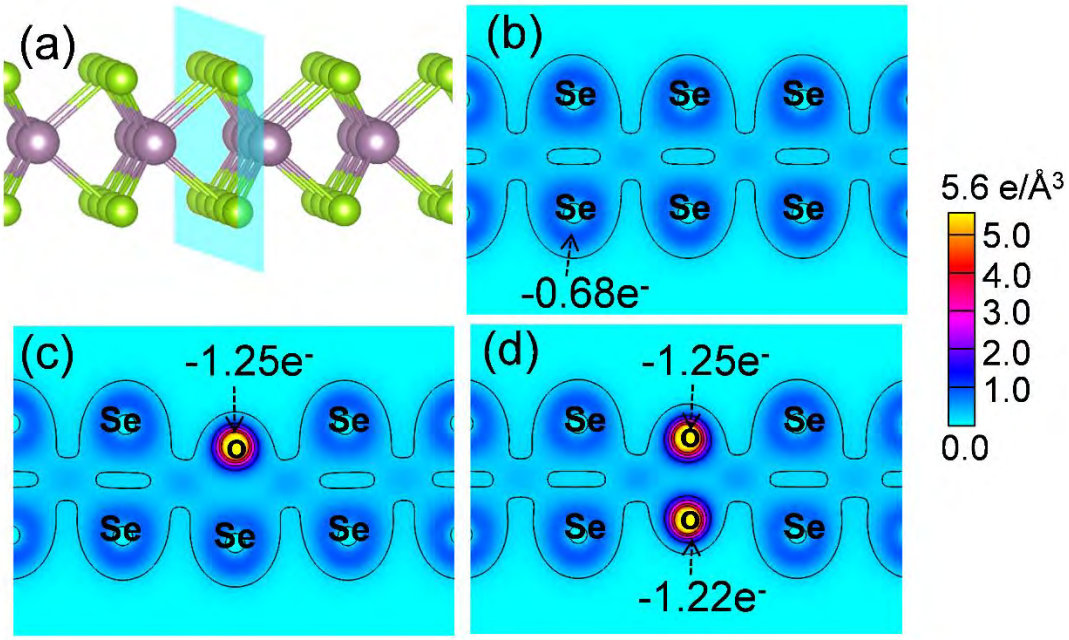

Figure S20. Electron density distributions: (a) Cross-section of the model, (b) Pristine $MoSe_2$, (c) $MoSe_2$ with one oxygen dopant, and (d) $MoSe_2$ with two oxygen dopants.

References

(1) Zhang, C.; Jiang, L.; Zhang, Y.; Hu, J.; Leung, M. K. H. Janus Effect of O_2 Plasma Modification on the Electrocatalytic Hydrogen Evolution Reaction of Mos_2. *J. Catal.* **2018**, 361, 384-392.

(2) Zhang, P.; Xiang, H.; Tao, L.; Dong, H.; Zhou, Y.; Hu, T. S.; Chen, X.; Liu, S.; Wang, S.; Garaj, S. Chemically Activated Mos2 for Efficient Hydrogen Production. *Nano Energy* **2019**, 57, 535-541.

(3) Nguyen, V. T.; Yang, T. Y.; Le, P. A.; Yen, P. J.; Chueh, Y. L.; Wei, K. H. New Simultaneous Exfoliation and Doping Process for Generating Mx2 Nanosheets for Electrocatalytic Hydrogen Evolution Reaction. *ACS Appl. Mater. Interfaces* **2019**, 11, 14786-14795.

(4) Li, S.; Zhou, S.; Wang, X.; Tang, P.; Pasta, M.; Warner, J. H. Increasing the Electrochemical Activity of Basal Plane Sites in Porous 3d Edge Rich Mos2 Thin Films for the Hydrogen Evolution Reaction. *Mater. Today Energy* **2019**, 13, 134-144.

(5) Cheng, C.-C.; Lu, A.-Y.; Tseng, C.-C.; Yang, X.; Hedhili, M. N.; Chen, M.-C.; Wei, K.-H.; Li, L.-J. Activating Basal-Plane Catalytic Activity of Two-Dimensional Mos2 Monolayer with Remote Hydrogen Plasma. *Nano Energy* **2016**, 30, 846-852.

(6) Xiao, D.; Ruan, Q.; Bao, D. L.; Luo, Y.; Huang, C.; Tang, S.; Shen, J.; Cheng, C.; Chu, P. K. Effects of Ion Energy and Density on the Plasma Etching-Induced Surface Area, Edge Electrical Field, and Multivacancies in $Mose_2$ Nanosheets for Enhancement of the Hydrogen Evolution Reaction. *Small* **2020**, 16, e2001470.

(7) Xia, B.; Wang, T.; Jiang, X.; Zhang, T.; Li, J.; Xiao, W.; Xi, P.; Gao, D.; Xue, D.; Ding, J. Ar^{2+} Beam Irradiation-Induced Multivancancies in $Mose_2$ Nanosheet for Enhanced Electrochemical Hydrogen Evolution. *ACS Energy Lett.* **2018**, 3, 2167-2172.

(8) Liu, T.; Liu, X.; Bhattacharya, S.; Ye, Z.; He, R.; Gao, X. P. A.; Akolkar, R.; Sankaran, R. M. Plasma-Induced Fabrication and Straining of Mos2 Films for the Hydrogen Evolution Reaction. *ACS Appl. Energ. Mater.* **2019**, 2, 5162-5170.

(9) Balasubramanyam, S.; Shirazi, M.; Bloodgood, M. A.; Wu, L.; Verheijen, M. A.; Vandalon, V.; Kessels, W. M. M.; Hofmann, J. P.; Bol, A. A. Edge-Site Nanoengineering of Ws2 by Low-Temperature Plasma-Enhanced Atomic Layer Deposition for Electrocatalytic Hydrogen Evolution. *Chem. Mater.* **2019**, 31, 5104-5115.